TECHNISCHE UNIVERSITÄT WIEN

DIPLOMARBEIT

Comparison of Different Models for the Design of Gas-Driven Fire Protection Systems: From Ideal Gas to Real Gas Models

zur Erlangung des akademischen Grades

Diplom-Ingenieur

im Rahmen des Studiums

Technische Physik

eingereicht von

Matthias Kronsteiner
Matrikelnummer 12009250

ausgeführt am Institut für Festkörperphysik
der Fakultät für Physik der Technischen Universität Wien
(in Zusammenarbeit mit AQUASYS TECHNIK GMBH)

Betreuung
Betreuer: Associate Prof. Dr. Alessandro Toschi
Mitwirkung: Dipl.-Ing. Lukas Heschl

Wien, 19.06.2025

(Unterschrift Verfasser) (Unterschrift Betreuer)

Die approbierte gedruckte Originalversion dieser Diplomarbeit ist an der TU Wien Bibliothek verfügbar
The approved original version of this thesis is available in print at TU Wien Bibliothek.
TU Bibliothek Your knowledge hub

Acknowledgments

First of all, I would like to express my sincere gratitude to my supervisor, Alessandro Toschi, for his guidance, help and constant support and effort throughout the research and writing of this thesis. Then I want to thank Lukas Heschl, Lukas Etzlstorfer and the entire AQUASYS TECHNIK GMBH for the opportunity to complete parts of this thesis under their guidance and the realization of the experiments in their facilities. Finally, I would like to thank my family, my friends and my fellow students for the great time and the support they have given me throughout my studies.

Die approbierte gedruckte Originalversion dieser Diplomarbeit ist an der TU Wien Bibliothek verfügbar
The approved original version of this thesis is available in print at TU Wien Bibliothek.

Abstract

For the design of a GPP (Gas-Powered Power Pack) firefighting system to be used in rail vehicles, it is legally required to exceed spraying pressure minima at all times throughout the spraying process. However, because of real gas effects, a purely analytical calculation of the time dependence of the pressure in the system is hardly possible and a trial-and-error approach during system construction is economically not feasible. In this thesis work, three models were developed to numerically simulate the temporal development of pressure and temperature of a simple GPP firefighting system. They were based, in order of increasing complexity, on the ideal gas law, the van der Waals gas law and a real gas description using an experimentally fitted Helmholtz equation of state as well as tabulated real gas data. While all models were able to capture the qualitative form of the pressure curves, as one expected, the real gas model yielded the best results when compared to two experiments specifically performed for the scope of this thesis with argon at different starting pressures. Due to approximations of the system geometry and neglected dynamic effects, even the real gas model displayed deviations with respect to the experiment. However, these errors appear to be small enough, to regard the real gas model as a promising approach toward the development of realistic simulation tools for the industrial system layout process.

Die approbierte gedruckte Originalversion dieser Diplomarbeit ist an der TU Wien Bibliothek verfügbar
The approved original version of this thesis is available in print at TU Wien Bibliothek.

Zusammenfassung

Für die Auslegung einer Brandbekämpfungsanlage mit einem Gas-Powered Power Pack (GPP) ist es aufgrund rechtlicher Vorgaben notwendig, während des Sprühvorgangs zu jedem Zeitpunkt einen minimalen Sprühdruck zu übertreffen. Wegen Realgaseffekten ist eine analytische Abschätzung jedoch kaum möglich und ein Trial-and-Error-Verfahren während der Konstruktion der Anlage wäre nicht wirtschaftlich. Deshalb wurden drei Modelle zur numerischen Simulation der zeitlichen Entwicklung von Druck und Temperatur einer einfachen GPP-Brandbekämpfungsanlage entwickelt. Diese basieren in aufsteigender Komplexität auf der idealen Gasgleichung, der van-der-Waals-Gleichung und einer Realgasbeschreibung, die eine an experimentelle Daten angepasste Helmholtz-Zustandsgleichung und tabellierte Realgasdaten verwendet. Alle Modelle waren in der Lage die qualitative Form der Druckkurven zu beschreiben. Das Realgasmodell wies jedoch, wie zu erwarten, eindeutig die besten Ergebnisse, im Vergleich zu zwei für diese Arbeit durchgeführten Experimenten mit Argon und unterschiedlichen Startdrücken, auf. Aufgrund von Näherungen in der Beschreibung der Systemgeometrie und der Vernachlässigung dynamischer Effekte war aber selbst das Realgasmodell nicht in der Lage, perfekte Vorhersagen zu liefern. Dennoch erscheinen die Fehler des Realgasmodells klein genug, sodass dieses als vielversprechender Ansatz zur Entwicklung von realistischeren Simulationsprogrammen, welche im industriellen Auslegungsprozess genutzt werden können, angesehen werden kann.

Die approbierte gedruckte Originalversion dieser Diplomarbeit ist an der TU Wien Bibliothek verfügbar
The approved original version of this thesis is available in print at TU Wien Bibliothek.

Contents

Die approbierte gedruckte Originalversion dieser Diplomarbeit ist an der TU Wien Bibliothek verfügbar
The approved original version of this thesis is available in print at TU Wien Bibliothek.
TU Bibliothek Your knowledge hub WIEN

Die approbierte gedruckte Originalversion dieser Diplomarbeit ist an der TU Wien Bibliothek verfügbar
The approved original version of this thesis is available in print at TU Wien Bibliothek.

1 Introduction

The safety of passengers and personnel is of the utmost importance in rail transportation. At the same time, economic as well as space constraints limit the size and weight of firefighting systems. Even so, manufacturers must comply with European and national regulations. A possibility of providing sufficient firefighting capability under these circumstances and constraints is given through the use of gas-powered power packs (GPP). These are systems where a high-pressure operating gas supplies the energy to power the firefighting process. In practice, they are based on the rapid expansion of the gas under high pressure. As this implies high densities, where interatomic forces play an important role, an analytical calculation of the temporal development of the pressure provided by the gas is not possible.

On the other hand, for a proper design and layout of the system, it is essential to know the value of the system pressure at any time. In this situation, a trial-and-error approach, in which the system would actually need to be built and adapted at the manufacturers facility could be in principle adopted. However, it is quiet evident that sucha procedure would not be economically feasible. Hence, a possible compromise consists in using a pressure reducing valve, which lowers the fire extinguishing capacity but enables the usage of analytical approximations for the spraying pressure, due to the nearly constant pressure applied on the water.

This approach is obviously not completely satisfactory either, as the full firefighting capability of a system will be then *not* exploited. The aim of this thesis is to evaluate whether a calculation exploiting a Euler timestepping approach and three different gas models is capable of yielding sufficiently accurate predictions to be used for the system design. The three models, listed in order of increasing complexity, are (i) the ideal gas, (ii) the van der Waals gas, and (iii) the real gas model, which exploits tabulated data and an empirically fitted Helmholtz equation of state.

The performance of these models for the problem of our interest are then evaluated by comparing the simulation values with the results of two experiments carried out in the facilities of AQUASYS TECHNIK GMBH in Linz, a high-pressure water mist firefighting system manufacturer. In particular, the results of all three models are discussed with regard to their ability to predict the temporal development of the system pressure and to approximate correctly the real gas effects.

Die approbierte gedruckte Originalversion dieser Diplomarbeit ist an der TU Wien Bibliothek verfügbar
The approved original version of this thesis is available in print at TU Wien Bibliothek.
TU Bibliothek Your knowledge hub WIEN

2 Firefighting in Rail Vehicles

This chapter introduces the reader to the legal requirements and other challenges of firefighting in rail vehicles in Section 2.1. In Section 2.2 the GPP, one possible firefighting system in trains is introduced and illustrated.

2.1 Special Requirements for Firefighting in Rail Vehicles

The most important objective of any firefighting system in rail vehicles is to ensure the safety of staff and passengers. In this perspective, a complete extinguishing of a fire is desirable, but not absolutely necessary. Above all, it is important to keep temperatures and smoke formation at such a low level over an extended period of time to allow for a safe evacuation of the train. In addition, there are specific legal and economical requirements that need to be considered.

2.1.1 Legal Requirements

Considering the European legislation is necessary due to the interconnectivity and interoperability of rail transport within the European Union. This not only provides union-wide safety standards but also technical standards to help manufacturers design their products. The legal framework is provided by the DIRECTIVE (EU) 2016/797 OF THE EUROPEAN PARLIAMENT AND OF THE COUNCIL of 11 May 2016 on the interoperability of the rail system within the European Union [1] that defines the subsystems of the European rail system and several Technical Specifications for Interoperability (TSI) that define technical and operational standards and requirements for those subsystems as explained in [2]. In addition, national requirements must be met. Very common guidelines that are often required to be met are the ARGE (Arbeitsgemeinschaft) guidelines defined by TÜV in Germany. For example, the second guideline [3] defines standards for the verification of function of firefighting systems in rail vehicles.

2.1.2 Economical Requirements

To ensure sufficient firefighting capability of a fire extinguishing system, one might initially consider to build larger, heavier and thus more powerful and longer lasting systems. However, there are several limitations to the size and weight of a firefighting system. First, the space in rail vehicles is intrinsically limited. Second, any additional weight, which has to be carried by a train over its entire life, means additional work, and therefore additional energy consumption. Thus, manufacturers aim at system dimensions as small as possible, while still being large enough to ensure adequate firefighting capability.

Die approbierte gedruckte Originalversion dieser Diplomarbeit ist an der TU Wien Bibliothek verfügbar
The approved original version of this thesis is available in print at TU Wien Bibliothek.
TU Bibliothek Your knowledge hub WIEN

2.2 Gas-Powered Power Packs

One solution to provide sufficient firefighting capability in limited space are gas-powered power packs, in short GPP. GPPs consist of one or more gas vessels filled with some gas, for example nitrogen, to very high pressures. In the event of a fire, a trigger valve is opened, and the gas expands through a pipe into one or more water vessels. The sudden pressure enhancement pushes the water through riser pipes into a piping system that leads to the nozzle head through which it is sprayed onto the fire. While the advantage of GPPs is arguably the small space requirement and low weight compared to other pressure sources, they have one major disadvantage. Due to the relevance of interatomic forces in these high pressure and high density settings it is impossible to analytically calculate the temporal development of the system pressure and thus the temporal development of the water spraying process. In fact, because of the rapid expansion and of the high pressure of the gas, real gas effects play a major role. This is a problem because regulations define minimum spraying pressures and spray times that must always be met by the system to be allowed for an actual usage. One way to solve this problem is to install a pressure reducing valve between the gas and water vessels. This leads to an approximately constant pressure applied to the water, as long as the gas pressure does not fall below the pressure defined by the valve. In this case however, this method has two disadvantages. First, the lower pressure applied to the water implies that the acceleration of the water through the piping system is slower and the water reaches the nozzle head later, leading to a significant delay in the start of spraying. Second, the system does not exploit its full potential in terms of spray pressure, which leads, in particular, to less water being sprayed at the beginning. Together, these two disadvantages significantly weaken the initial firefighting capability, possibly allowing the fire to spread further, damage the train, and threaten the lives of passengers. Despite these disadvantages, however, pressure reducing valves are still commonly used in practice due to the fact that the alternative trial-and-error method to design a high-pressure system without it is too elaborate and expensive.

Die approbierte gedruckte Originalversion dieser Diplomarbeit ist an der TU Wien Bibliothek verfügbar
The approved original version of this thesis is available in print at TU Wien Bibliothek.
TU Bibliothek Your knowledge hub WIEN

3 Statistical Physics

This chapter gives an introduction and an overview of the thermodynamics formalism relevant to this thesis. In particular, Section 3.1 summarizes the laws of thermodynamics, and in Section 3.2 the ideal gas equation is derived following the approach in [4]. Then, the virial expansion of the ideal gas law is shown in Section 3.3. Starting from this, the van der Waals equation is subsequently derived in Section 3.4. The virial expansion and derivation of the van der Waals equation follow the lecture slides [5] that use [6], [7], [8] and [9] as sources. An approach to calculate the Helmholtz energy for a real gas following [10] is given in Section 3.5. Finally, convective heat transfer, as used in [11], is discussed in Section 3.6.

3.1 Laws of Thermodynamics

The four laws of thermodynamics are empirically found scientific laws that appear to be true for all thermodynamical systems at all times.

3.1.1 Zeroth Law

Two physical systems are in thermal equilibrium if there is no net energy transfer between them when they are connected by a path of possible heat exchange. The zeroth law states:

> *If a thermodynamical system A is in thermal equilibrium with a thermodynamical system B and if this thermodynamical system B is in thermal equilibrium with a thermodynamical system C, then A and C are also in thermal equilibrium.*

3.1.2 First Law

The first law of thermodynamics is the thermodynamic equivalent of the conservation of energy. It states that:

> *Any change of inner energy of the system can only happen by transport of energy as work or heat through the boundaries of the system.*

Mathematically, this can be written as

$$\mathrm{d}U = \delta Q + \delta W \tag{3.1}$$

with the differential inner energy $\mathrm{d}U$, the differential heat flow δQ and the differential work δW. Note that we use a d for the differential energy because it is a state function and δ for the differential heat and work because they are process functions. Here, the sign conventions are important in the definition. With the definition in (3.1), δQ is

Die approbierte gedruckte Originalversion dieser Diplomarbeit ist an der TU Wien Bibliothek verfügbar
The approved original version of this thesis is available in print at TU Wien Bibliothek.
TU Bibliothek Your knowledge hub WIEN

positive when heat flows into the system and δW when work is done on the system by the surroundings. We note here that since the inner energy is one of the two quantities used to calculate the new state after a time step, the first law is of great importance for this thesis.

3.1.3 Second Law

The first law of thermodynamics would allow processes that are not observed in the real world. For example, in our case, the net gas flow will always be from the vessel with higher pressure to the vessel with lower pressure. The reverse process, in which more gas flows from the low-pressure vessel to the high-pressure vessel increasing the pressure difference, will not occur, although it would be, in principle, not forbidden by the law of energy conservation. Such processes of systems going spontaneously from a unordered state to a more ordered state are prohibited by the second law of thermodynamics. The second law of thermodynamics is a consequence of probability and statistics. As there are far more possible configurations that represent a macroscopically unordered state than the ordered one, it is just far more likely that in thermal equilibrium a system will be in an unordered state. To quantify this concept at a microscopical level, one can define the entropy S by

$$S = k_B \ln(w) \tag{3.2}$$

with the Boltzmann constant k_B and the probability that the system is in the macroscopic state w, which can be calculated by dividing the number of microscopic states that represent the corresponding macroscopic state by the number of all possible states. Now, the second law of thermodynamics states that:

In a closed system spontaneously happening processes (also called irreversible processes) always lead to an increase in total entropy.

3.1.4 Third Law

Although it is not important for this thesis, for the sake of completeness, the third law shall also be mentioned. In its historical formulation it states that

$$\lim_{T \to 0} S(T) = 0, \tag{3.3}$$

or in words:

It is impossible to reach a temperature of 0 Kelvin by a finite set of thermodynamical transformations.

Die approbierte gedruckte Originalversion dieser Diplomarbeit ist an der TU Wien Bibliothek verfügbar
The approved original version of this thesis is available in print at TU Wien Bibliothek.
TU Bibliothek Your knowledge hub WIEN

3.2 Ideal Gas Model

The ideal gas law can be derived from the kinetic gas theory. This derivation follows the steps presented in [4]. The starting point is a gas with infinitesimally small atoms that do not interact with each other. The pressure p applied by the gas on the container wall can be then readily defined as

$$p = \frac{F}{A} = \frac{1}{A}\frac{\mathrm{d}}{\mathrm{d}t}p_\perp \tag{3.4}$$

with A being the respective surface of the wall and $p_\perp$ the impulse of the wall orthogonal to its surface. Assuming that all atoms have the velocity $v_\perp$ orthogonal to the wall surface and that only elastic collisions occur, $p_\perp$ can be calculated,

$$p_\perp = 2Nmv_\perp \tag{3.5}$$

with N being the number of atoms that collide with the wall and m the mass of the atoms. This leads to

$$p = \frac{\mathrm{d}}{\mathrm{d}t}\frac{2Nmv_\perp}{A} \ . \tag{3.6}$$

The number of particles colliding with the wall can be calculated as the product of the wall area with the velocity of the particles, their density n and a small time increment:

$$N = nAv_\perp \mathrm{d}t \ . \tag{3.7}$$

Thus, the pressure can be written as

$$p = \frac{\mathrm{d}}{\mathrm{d}t}\frac{2nAv_\perp \mathrm{d}tmv_\perp}{A} = 2nmv_\perp^2 \ . \tag{3.8}$$

This definition still has two flaws: First, not all particles have the exact same square velocity $v_\perp^2$ but the average

$$\left\langle v_\perp^2 \right\rangle = \frac{1}{N}\int N(v_\perp)\ v_\perp^2\ \mathrm{d}v_\perp \tag{3.9}$$

should be used. Second, only half the density contributes since approximately half of the particles will travel in the opposite direction. Thus, the expression for the pressure further simplifies to:

$$p = nm\left\langle v_\perp^2 \right\rangle \ . \tag{3.10}$$

Since the directions of the velocities will be equally distributed in all spatial directions,

Die approbierte gedruckte Originalversion dieser Diplomarbeit ist an der TU Wien Bibliothek verfügbar
The approved original version of this thesis is available in print at TU Wien Bibliothek.

one can further assume that

$$\left\langle v_{\perp}^2 \right\rangle = \frac{1}{3} \left\langle v^2 \right\rangle \ , \tag{3.11}$$

and write the pressure as

$$p = \frac{1}{3} mn \left\langle v^2 \right\rangle = \frac{2}{3} n \left\langle E_{kin} \right\rangle \ . \tag{3.12}$$

With the definition of absolute temperature from [4] as

$$\frac{3}{2} k_B T = \left\langle E_{kin} \right\rangle \ , \tag{3.13}$$

which could also be proven with the euqipartition theorem or the virial theorem, one gets the ideal gas law

$$p = n k_B T \ , \tag{3.14}$$

or when using the number of particles instead of the density:

$$pV = N k_B T \ . \tag{3.15}$$

3.3 Virial Expansion

For the derivation of the ideal gas law, interactions between particles are completely neglected. However, since the process studied in this thesis occurs under high-pressure and high-density conditions, particle interactions should be expected to play a major role. Thus, a Hamiltonian of form

$$H = \sum_{i=1}^{N} \frac{\vec{p}_i^{\,2}}{2m} + \frac{1}{2} \sum_{i,j=1, i \neq j}^{N} U(\vec{x}_i - \vec{x}_j) \tag{3.16}$$

with the the momentum of the i-th particle $\vec{p}_i$ and a two particle interaction U should be considered. A common way to take interactions into account is the virial expansion of the ideal gas law. This is an expansion of the ideal gas law in powers of the particle density n:

$$\frac{p}{k_B T} = n + B_2(T)\ n^2 + B_3(T)\ n^3 + \ \ldots \ = \sum_{i=1}^{\infty} B_n(T)\ n^i \ , \tag{3.17}$$

where, the lowest order term $B_1(T)$, which describes the ideal gas law in the $n \to 0$ limit, is one.

Die approbierte gedruckte Originalversion dieser Diplomarbeit ist an der TU Wien Bibliothek verfügbar
The approved original version of this thesis is available in print at TU Wien Bibliothek.
TU Bibliothek Your knowledge hub WIEN

Starting point of the corresponding derivation is the grand canonical partition function

$$Z_G = \sum_{N=0}^{\infty} e^{\beta\mu N} \; Z_K(N) \tag{3.18}$$

where

$$\beta = \frac{1}{k_B T} \; , \tag{3.19}$$

the canonical partition function $Z_K(N)$ reads

$$Z_K(N) = \frac{1}{N! h^{3N}} \int e^{\sum_{i=1}^{N} \frac{\vec{p}_i^2}{2m} + \frac{1}{2} \sum_{i,j=1, i \neq j}^{N} U(\vec{x_i} - \vec{x_j})} d^3x_1 \; ... \; d^3x_N \; d^3p_1 \; ... \; d^3p_N \tag{3.20}$$

and μ is the the chemical potential. With the grand canonical partition function, the grand canonical potential can be then directly calculated:

$$J(T, V, \mu) = -k_B T \ln(Z_G) = -pV \tag{3.21}$$

In particular, for our scopes, it is convenient to exploit the Taylor expansion for the logarithm

$$\ln(1 + x) = -\sum_{i=1}^{\infty} \frac{(-1)^i x^i}{i} \tag{3.22}$$

so that the grand canonical potential can be expanded into

$$J(T, V, \mu) = -k_B T \ln(Z_G) \tag{3.23}$$

$$= -k_B T \ln\left(1 + \sum_{N=1}^{\infty} e^{\beta\mu N} \; Z_K(N)\right) \tag{3.24}$$

$$= -k_B T [Z_K(1) \; e^{\beta\mu} + (Z_K(2) - \frac{Z_K^2(1)}{2}) \; e^{2\beta\mu}] + ... \; . \tag{3.25}$$

The next step is to find an approximation of $e^{\beta\mu}$ by the average particle number $\overline{N}$. To that end, the derivative of J with respect to μ can be calculated as

Die approbierte gedruckte Originalversion dieser Diplomarbeit ist an der TU Wien Bibliothek verfügbar
The approved original version of this thesis is available in print at TU Wien Bibliothek.
TU Bibliothek Your knowledge hub WIEN

$$\overline{N} = -\frac{\partial J}{\partial \mu} \tag{3.26}$$

$$= Z_K(1)\ e^{\beta\mu} + 2(Z_K(2) - \frac{Z_K(1)^2}{2})\ e^{2\beta\mu} + ... \tag{3.27}$$

$$\tag{3.28}$$

By iteratively solving for $e^{\beta\mu}$ using a power series ansatz, one gets

$$e^{\beta\mu} = \frac{\overline{N}}{Z_K(1)} - \frac{2\overline{N}^2}{Z_K^3(1)}\left[Z_K(2) - \frac{Z_K^2(1)}{2}\right] + ... \ . \tag{3.29}$$

Inserting this into the expression for J, which is equal to $-pV$, gives

$$pV = k_B T(\overline{N} - \frac{\overline{N}^2}{Z_K^2(1)}\left[Z_K(2) - \frac{Z_K^2(1)}{2}\right] + \mathcal{O}(\overline{N}^3)\ . \tag{3.30}$$

Rearranging this equation yields the virial expansion

$$\frac{p}{k_B T} = n - \frac{V}{Z_K^2(1)}\left[Z_K(2) - \frac{Z_K^2(1)}{2}\right]\ n^2 + \mathcal{O}(n^3) \tag{3.31}$$

$$= n + V\left[\frac{1}{2} - \frac{Z_K(2)}{Z_K^2(1)}\right]\ n^2 + +\mathcal{O}(n^3)\ . \tag{3.32}$$

3.4 Van der Waals Gas Model

Remarkably, already the inclusion of the first correction of the virial expansion in the form of the coefficient $B_2(T)$ yields a great improvement to the ideal gas law. To that end, the canonical partition functions for one and two particles need to be calculated:

$$Z_K(1) = \frac{1}{h^3}\prod_{i=1}^{3}\int e^{\frac{p_i^2}{2m}} dp_i \int d^3x = \frac{V}{\lambda_T^3}\ . \tag{3.33}$$

Here, λ_T is the thermal wavelength, defined as:

$$\lambda_T = \sqrt{\frac{h^2}{2\pi m k_B T}}\ . \tag{3.34}$$

The two particle canonical partition function can be then directly evaluated starting by its microscopical definitions:

Die approbierte gedruckte Originalversion dieser Diplomarbeit ist an der TU Wien Bibliothek verfügbar
The approved original version of this thesis is available in print at TU Wien Bibliothek.
TU Bibliothek Your knowledge hub WIEN

$$Z_K(2) = \frac{1}{2h^6} \prod_{i=1}^{6} \int dp_i \int d^3x_1 d^3x_2 \; e^{-\beta \; U(\vec{x}_1 - \vec{x}_2)} \tag{3.35}$$

$$= \frac{1}{2\lambda_T^6} \int d^3x_1 d^3x_2 \; e^{-\beta \; U(\vec{x}_1 - \vec{x}_2)} \; . \tag{3.36}$$

With these two expressions, the coefficient $B_2(T)$ can be calculated:

$$B_2(T) = V \left[\frac{1}{2} - \frac{Z_K(2)}{Z_K^2(1)} \right] \tag{3.37}$$

$$= V \left[\frac{1}{2} - \frac{1}{2V^2} \int d^3x_1 d^3x_2 \; e^{-\beta \; U(\vec{x}_1 - \vec{x}_2)} \right] \tag{3.38}$$

$$= -\frac{1}{2V} \int d^3x_1 d^3x_2 \; \left[e^{-\beta \; U(\vec{x}_1 - \vec{x}_2)} - 1 \right] \; . \tag{3.39}$$

To further simplify this expression, the substitution

$$\vec{x} = \vec{x}_1 - \vec{x}_2 \tag{3.40}$$

is used to get

$$B_2(T) = -\frac{1}{2V} \int d^3x_2 \int d^3x \; (e^{-\beta \; U(\vec{x})} - 1) \tag{3.41}$$

$$= -\frac{1}{2} \int d^3x \; (e^{-\beta \; U(\vec{x})} - 1) \; . \tag{3.42}$$

This integral would still be difficult to calculate for true atomic potentials. Thus, to get a first insight, the hard-sphere model is often used, where U is set to plus infinity if the particles come closer than the sum of the radii of both spheres r_0 and to a very small negative value elsewhere. With this model, the integral for $B_2(T)$ is separated into two parts. First, for all $\vec{x}$ with norm smaller than r_0, the exponential function vanishes and the integral evaluates to:

$$-\frac{1}{2} \int_{||\vec{x}|| < r_0} d^3x \; (e^{-\beta \; U(\vec{x})} - 1) = 2\pi \int_0^{r_0} dr \; r^2 = \frac{2\pi r_0^3}{3} = b \; . \tag{3.43}$$

For all $\vec{x}$ with greater norm U is assumed to be small and thus a Taylor expansion of the exponential function can be made:

Die approbierte gedruckte Originalversion dieser Diplomarbeit ist an der TU Wien Bibliothek verfügbar
The approved original version of this thesis is available in print at TU Wien Bibliothek.
TU Bibliothek Your knowledge hub WIEN

$$-\frac{1}{2}\int_{||\vec{x}||>r_0} d^3x\ (e^{-\beta\ U(\vec{x})}-1) \tag{3.44}$$

$$=-2\pi\int_{r_0}^{\infty} dr\ r^2(1-\beta U-1) \tag{3.45}$$

$$=\frac{2\pi}{k_BT}\int_{r_0}^{\infty} dr\ r^2\ U \tag{3.46}$$

$$=-\frac{a}{k_BT}\ . \tag{3.47}$$

The parameter a is defined as negative, since U is assumed to be negative for $|r| > r_0$. Now, with these values, one can write the second virial coefficient

$$B_2(T)=b-\frac{a}{k_BT}\ , \tag{3.48}$$

in terms of the parameter a and b, which, in practice, are typically experimentally determined for each gas. Inserting these values back into the virial expansion, one gets:

$$\frac{p}{k_BT}=n+\left(b-\frac{a}{k_BT}\right)\ n^2 \tag{3.49}$$

$$=\frac{1}{\bar{v}}+\left(b-\frac{a}{k_BT}\right)\frac{1}{\bar{v}^2}\ , \tag{3.50}$$

where $\bar{v}$ is the volume per particle:

$$\bar{v}=\frac{V}{N}\ . \tag{3.51}$$

Equation (3.50) can be rearranged to

$$p+\frac{a}{\bar{v}^2}=\left(\frac{1}{\bar{v}}+\frac{b}{\bar{v}^2}\right)k_BT \tag{3.52}$$

$$\left(p+\frac{a}{\bar{v}^2}\right)\ \bar{v}\frac{1}{1+\frac{b}{\bar{v}}}=k_BT\ . \tag{3.53}$$

Using Taylor expansion for the fraction on the left-hand side yields:

Die approbierte gedruckte Originalversion dieser Diplomarbeit ist an der TU Wien Bibliothek verfügbar
The approved original version of this thesis is available in print at TU Wien Bibliothek.
TU Bibliothek Your knowledge hub WIEN

$$\left(p + \frac{a}{\bar{v}^2}\right)\ \bar{v}\left(1 - \frac{b}{\bar{v}}\right) = k_B T \tag{3.54}$$

$$\left(p + \frac{a}{\bar{v}^2}\right)(\bar{v} - b) = k_B T \tag{3.55}$$

Equation (3.55) is the well-known van der Waals equation, which is also commonly expressed using the molar volume

$$v_m = \frac{V}{n_m}\ , \tag{3.56}$$

where n_m is the number of moles in the gas that can be calculated through division of the number of particles N by the Avogadro constant N_A:

$$n_m = \frac{N}{N_A}\ . \tag{3.57}$$

With this definition the van der Waals equation can be written as

$$(p + \frac{a}{v_m^2})(v_m - b) = RT\ , \tag{3.58}$$

where R is the molar gas constant:

$$R = N_A\ k_B\ . \tag{3.59}$$

We recall that Equation (3.58) could also be derived by using a cluster expansion or a mean-field approach to calculate the free energy.

In any case, from a physical point of view, the coefficient a represents an effective description of the attractive interaction between the particles, which reduces the pressure compared to the ideal gas pressure. The coefficient b accounts effectively for the strong repulsive effects on short distances in terms of the "finite volume" of the gas particles. Evidently this reduces the volume available for the gas particles increasing the pressure compared to the ideal gas. The coefficients for the argon gas, which were used in this

Die approbierte gedruckte Originalversion dieser Diplomarbeit ist an der TU Wien Bibliothek verfügbar
The approved original version of this thesis is available in print at TU Wien Bibliothek.
TU Bibliothek Your knowledge hub WIEN

thesis

$$a = 0.1355 \, \frac{\mathrm{Pa} \cdot \mathrm{m}^6}{\mathrm{mol}^2} \tag{3.60}$$

$$b = 3.2 \cdot 10^{-5} \, \frac{\mathrm{m}^3}{\mathrm{mol}} \tag{3.61}$$

were taken from [12].

For the inner energy of the van der Waals gas, the Legendre transformation to the Helmholtz energy with differential

$$dF = -S \, dT - p \, dV = \left.\frac{\partial F}{\partial T}\right|_V dT + \left.\frac{\partial F}{\partial V}\right|_T dV \tag{3.62}$$

is considered. From Schwartz's Theorem

$$\frac{\partial^2 f(x,y)}{\partial x \partial y} = \frac{\partial^2 f(x,y)}{\partial y \partial x} \tag{3.63}$$

follows that

$$\left.\frac{\partial S}{\partial V}\right|_T = \left.\frac{\partial p}{\partial T}\right|_V \, . \tag{3.64}$$

Thus, the partial derivative of the inner energy with respect to the volume is

$$\left.\frac{\partial U}{\partial V}\right|_T = T \left.\frac{\partial S}{\partial V}\right|_T - p \tag{3.65}$$

$$= T \left.\frac{\partial p}{\partial T}\right|_V - p \, . \tag{3.66}$$

For the ideal gas one gets

$$\left.\frac{\partial p}{\partial T}\right|_V = \frac{N \, k_B}{V} = \frac{p}{T} \, . \tag{3.67}$$

Inserting this solution back into Equation (3.66) yields for the ideal gas

$$\left.\frac{\partial U}{\partial V}\right|_T = 0 \, . \tag{3.68}$$

This shows that for the ideal gas the inner energy does *not* depend on the volume, but only on the temperature.

Die approbierte gedruckte Originalversion dieser Diplomarbeit ist an der TU Wien Bibliothek verfügbar
The approved original version of this thesis is available in print at TU Wien Bibliothek.
TU Bibliothek Your knowledge hub WIEN

At the same time, for the van der Waals gas the derivative of the pressure with respect to the temperature yields

$$\left.\frac{\partial p}{\partial T}\right|_V = \frac{R}{v_m - b} \ . \tag{3.69}$$

Inserting this solution back into Equation (3.66) one gets the following expression:

$$\left.\frac{\partial U}{\partial V}\right|_T = \frac{R\ T}{v_m - b} - \frac{R\ T}{v_m - b} + \frac{a}{v_m^2} \tag{3.70}$$

$$= \frac{a}{v_m^2} \ . \tag{3.71}$$

Thus, the inner energy of a van der Waals gas with volume V in reference to the inner energy of the ideal gas U_{ideal} is given by

$$U = U_{\text{ideal}} + \int_\infty^V \left.\frac{\partial U}{\partial V}\right|_T \, dV \tag{3.72}$$

$$= U_{\text{ideal}} + \int_\infty^V \frac{a\ n_m^2}{V^2} \, dV \tag{3.73}$$

$$\tag{3.74}$$

$$= U_{\text{ideal}} - \frac{a\ n_m^2}{V} \ . \tag{3.75}$$

The here presented derivation of Equation (3.75) is taken from [12].

3.5 Helmholtz Equation of State

An even more advanced method to account for real gas behavior in thermodynamical calculations is to calculate the Helmholtz energy and, then, to compute thermodynamical quantities as derivatives of this state function. Because the gas used for this thesis is argon, the approach taken to calculate the Helmholtz energy presented in this chapter is, as already mentioned, taken from [10]. The resulting equation of state is also the one exploited in the CoolProp Python package [13], which is actually used to calculate the values in the implementation.

For the ideal gas, the Helmholtz energy per mole with the two independent variables density ρ and temperature T is given by

Die approbierte gedruckte Originalversion dieser Diplomarbeit ist an der TU Wien Bibliothek verfügbar
The approved original version of this thesis is available in print at TU Wien Bibliothek.

$$F^0(\rho,T) = u^0(T) - Ts^0(\rho,T) \tag{3.76}$$
$$= h^0(T) - pV - Ts^0(\rho,T) \tag{3.77}$$
$$= h^0(T) - RT - Ts^0(\rho,T)\ , \tag{3.78}$$

with the ideal gas molar inner energy u^0, the ideal gas molar entropy s^0, the ideal gas molar enthalpy h^0 and the universal gas constant R. Typically, the dimensionless version of this quantity

$$\alpha^0(\delta,\tau) = \frac{F^0(\rho,T)}{RT} \tag{3.79}$$

is used, where δ is the reduced density,

$$\delta = \frac{\rho}{\rho_c}\ , \tag{3.80}$$

with the density at the critical point ρ_c and τ is the inverse reduced temperature,

$$\tau = \frac{T_c}{T}\ , \tag{3.81}$$

with the temperature at the critical point T_c. To account for real gas behavior, the difference between the ideal gas Helmholtz energy and the true Helmholtz energy, which in the following we will call residual Helmholtz energy α^r, needs to be considered:

$$\alpha(\delta,\tau) = \alpha^0(\delta,\tau) + \alpha^r(\delta,\tau) \tag{3.82}$$

For the ideal gas Helmholtz energy, for which an analytical calculation is possible, a point of reference for both thermodynamical potentials h^0 and s^0 is needed. For this thesis, the potentials are set to zero for standard ambient temperature T_0 and pressure p_0 being 25 °C and one bar following the definitions in [10]. Then one can calculate the enthalpy correspondingly by

$$h^0(T) = c_p^0(T - T_0) \tag{3.83}$$
$$= T\ c_p^0(1 - \frac{T_0}{T_c}\tau)\ , \tag{3.84}$$

with the molar heat capacity at constant pressure c_p^0 being 2.5 R. Let ρ_0 be the density at T_0 and p_0, then, the entropy is given by:

Die approbierte gedruckte Originalversion dieser Diplomarbeit ist an der TU Wien Bibliothek verfügbar
The approved original version of this thesis is available in print at TU Wien Bibliothek.
TU Bibliothek Your knowledge hub WIEN

$$s^0(\rho,T) = c_V^0 \ln\frac{T}{T_0} + R\ln\frac{V}{V_0} \tag{3.85}$$
$$= (c_p^0 - R)\ln\frac{T}{T_0} + R\ln\frac{\rho_0}{\rho} \tag{3.86}$$
$$= -(c_p^0 - R)\ln\left(\frac{T_0}{T_c}\frac{T_c}{T}\right) - R\ln\left(\frac{\rho_c}{\rho_0}\frac{\rho}{\rho_c}\right) \tag{3.87}$$
$$= -(c_p^0 - R)(\ln\frac{T_0}{T_c} + \ln\tau) - R(\ln\frac{\rho_c}{\rho_0} + \ln\delta)\ . \tag{3.88}$$
$$\tag{3.89}$$

In the third row above we just multiply the arguments of the logarithms by $\frac{T_c}{T_c} = 1$ and $\frac{\rho_c}{\rho_c} = 1$ respectively. Thus, for the dimensionless Helmholtz energy of the ideal gas, one gets:

$$\alpha^0(\delta,T) = \frac{c_p^0}{R} - \frac{c_p^0}{R}\frac{T_0}{T_c}\tau - 1 + \left[\frac{c_p^0}{R} - 1\right]\ln\frac{T_0}{T_c} + \left[\frac{c_p^0}{R} - 1\right]\ln\tau + \ln\frac{\rho_c}{\rho_0} + \ln\delta \tag{3.90}$$
$$= 1.5\left[1 + \ln\frac{T_0}{T_c}\right] + \ln\frac{\rho_c}{\rho_0} - \frac{c_p^0}{R}\frac{T_0}{T_c}\tau + 1.5\ln\tau + \ln\delta \tag{3.91}$$
$$= a_1^0 + a_2^0\tau + 1.5\ln\tau + \ln\delta \tag{3.92}$$

With the critical temperature of argon at $T_c = 150.86$ K, the critical density at $\rho_c = 535.6\ \frac{\text{kg}}{\text{m}^3}$ and the density at T_0 and p_0 of $\rho_0 = 1.63\ \frac{\text{kg}}{\text{m}^3}$ the evaluation of the coefficients gives:

$$a_1^0 = +8.317\ , \tag{3.93}$$
$$a_2^0 = -4.947\ . \tag{3.94}$$

For the residual part, a large amount of experimental data was examined that led the authors of [10] to the following empirical form:

$$\alpha^r = \sum_{i=1}^{12} n_i\delta^{d_i}\tau^{t_i} + \sum_{i=13}^{37} n_i\delta^{d_i}\tau^{t_i}e^{-\delta^{c_i}} + \sum_{i=38}^{41} n_i\delta^{d_i}\tau^{t_i}e^{-\eta_i(\delta-\epsilon_i)^2-\beta_i(\tau-y_i)^2}\ . \tag{3.95}$$

In particular, the parameters were fitted with a nonlinear regression analysis to the experimental data and are displayed in [10]. The expression for the total Helmholtz energy is then valid for the entire region covered by the experimental data, which is

Die approbierte gedruckte Originalversion dieser Diplomarbeit ist an der TU Wien Bibliothek verfügbar
The approved original version of this thesis is available in print at TU Wien Bibliothek.

$$83.8058 \text{ K} \leq T \leq 700 \text{ K} ,$$
$$0 \text{ MPa} \leq p \leq 1000 \text{ MPa} .$$

Thus, it covers the whole region relevant for this thesis. Now other thermodynamic quantities can be easily calculated using the Helmholtz energy and its derivatives. For this thesis, the relevant quantities are the pressure

$$\frac{p}{\rho RT} = -\frac{1}{\rho RT}\frac{\partial}{\partial v}F \tag{3.96}$$
$$= -\frac{1}{\rho}\frac{\partial}{\partial v}\alpha \tag{3.97}$$
$$= \rho\frac{\partial}{\partial \rho}\alpha \tag{3.98}$$
$$= \delta\frac{\partial}{\partial \delta}\alpha \tag{3.99}$$
$$= 1 + \delta\frac{\partial}{\partial \delta}\alpha^r , \tag{3.100}$$

the molar inner energy

$$\frac{u}{RT} = \frac{1}{RT}(F + Ts) \tag{3.101}$$
$$= \frac{1}{RT}\left(F - T\frac{\partial F}{\partial T}\right) \tag{3.102}$$
$$= \alpha - \frac{1}{R}\frac{\partial}{\partial T}(RT\alpha) \tag{3.103}$$
$$= \alpha - \frac{1}{R}(R\alpha + RT\frac{\partial}{\partial T}\alpha) \tag{3.104}$$
$$= \frac{T_c}{T}\frac{\partial}{\partial \tau}\alpha \tag{3.105}$$
$$= \tau\frac{\partial}{\partial \tau}\alpha , \tag{3.106}$$

and the molar enthalpy

Die approbierte gedruckte Originalversion dieser Diplomarbeit ist an der TU Wien Bibliothek verfügbar
The approved original version of this thesis is available in print at TU Wien Bibliothek.

$$\frac{h}{RT} = \frac{1}{RT}(F - Ts - pv) \tag{3.107}$$

$$= \frac{u}{RT} + \frac{p}{\rho RT} \tag{3.108}$$

$$= \tau \frac{\partial}{\partial \tau}\alpha + 1 + \delta \frac{\partial}{\partial \delta}\alpha^r \ . \tag{3.109}$$

It is worth to mention here, that in the algorithm used in this thesis, it is not τ and δ that are calculated in each time step, but u and δ. Thus, τ has to be calculated iteratively.

3.6 Heat Transfer

Through expansion, the gas in the gas vessel of our system (see Section 7) is expected to cool considerably. This can also be seen in experiments with the naked eye, as the water from the ambient air starts to condense on the gas vessel. Thus, a large amount of heat is likely to flow into the gas through the gas vessel wall, increasing the inner energy. In this thesis, the heat flow will modeled by

$$\Delta Q = \kappa \ A \ \Delta T \ \Delta t \ , \tag{3.110}$$

with κ being the convective heat transfer coefficient, A the surface area normal to the direction of heat transfer, ΔT the temperature difference between the vessel wall and the fluid and Δt the duration of the time step. In particular, for a quantitatively accurate description, for heat transfer between the vessel wall and ambient air, setting κ to the specific value of 11 $\frac{\mathrm{W}}{\mathrm{m^2K}}$ has yielded good results. This value is an approximation based on the range of possible values for free convection in gases given in [14]. In the case of free convection, the gas only moves due to temperature differences, that are caused by the convection, which is the case for ambient air. If there is movement in the gas or fluid caused by any other force, then it is forced convection, which typically has higher heat transfer coefficients. For the discharging gas in the gas vessel, the gas moves almost exclusively due to the pressure difference. In this case, the convective heat transfer coefficient is approximated by calculating the Nusselt number

$$\mathrm{Nu} = \frac{\kappa l}{k} \ , \tag{3.111}$$

where l is the characteristic length of the vessel and k the thermal conductivity of the gas. For vertical vessels l was approximated to be the fluids share of the vessel length. An approximation of the Nusselt number is given in [15] by

Die approbierte gedruckte Originalversion dieser Diplomarbeit ist an der TU Wien Bibliothek verfügbar
The approved original version of this thesis is available in print at TU Wien Bibliothek.

$$\mathrm{Nu} = 0.13\mathrm{Ra}^{0.333} \qquad \forall\ \mathrm{Ra} > 10^9\ , \tag{3.112}$$

$$\mathrm{Nu} = 0.59\mathrm{Ra}^{0.25} \qquad \forall\ 10^4 < \mathrm{Ra} < 10^9\ , \tag{3.113}$$

$$\mathrm{Nu} = 1.36\mathrm{Ra}^{0.2} \qquad \forall\ \mathrm{Ra} < 10^4\ , \tag{3.114}$$

where Ra is the Rayleigh number that can be calculated by

$$\mathrm{Ra} = \mathrm{Gr}\ \mathrm{Pr} \tag{3.115}$$

with the Grashof number

$$\mathrm{Gr} = \frac{\tilde{\beta} g \rho^2 L^3 \Delta T}{\eta^2} \tag{3.116}$$

and the Prandtl number

$$\mathrm{Pr} = \frac{c_p \eta}{k}\ , \tag{3.117}$$

where $\tilde{\beta}$ is the volume expansion coefficient, g is the free fall acceleration and η is the dynamic viscosity. In particular, the value of $\tilde{\beta}$ can be obtained by deriving the equation of state while k and η are taken from [16]. The use of a single Nusselt number for the entire gas is evidently an approximation, as is experimentally shown in [17]. In this framework, all necessary values are calculated for a gas with the pressure of the gas interior and a temperature, which corresponds to the average of the gas bulk temperature and the vessel wall temperature. For the ideal gas model and the van der Waals gas model, where one has, obviously, no access to tabulated real gas data, the values were again approximated based on the given range of values for forced convection in gases and liquids in [14]. The values for the inner κ were set to 100 $\frac{\mathrm{W}}{\mathrm{m^2K}}$ for the gas, while for water it was set to 1000 $\frac{\mathrm{W}}{\mathrm{m^2K}}$.

Die approbierte gedruckte Originalversion dieser Diplomarbeit ist an der TU Wien Bibliothek verfügbar
The approved original version of this thesis is available in print at TU Wien Bibliothek.
TU Bibliothek Your knowledge hub WIEN

4 Fluid Dynamics

This chapter gives an overview of the formulas for modeling the flow of gas and water in the system. In particular, Section 4.1 introduces a formula for calculating the flow of gas through an orifice. In Section 4.2 a formula for the flow of water through an orifice or a nozzle head is derived using the Bernoulli equation. Finally, Section 4.3 introduces the reader to the Darcy-Weisbach equation and the calculation of the friction factor to compute the pressure loss for water flowing through a piping system.

4.1 Gas Outflow

The gas outflow from the gas vessel is modeled by the flow through an orifice, as described in [11], which is based on [18]. Following their derivations, the mass flow through an orifice that separates a gas with pressure p_1 and density ρ_1 from a gas with lower pressure p_2 is given by

$$\dot{m} = C_d \; A \; \psi \; \sqrt{\rho_1 \; p_1 \; \gamma (\frac{2}{\gamma + 1})^{\frac{\gamma+1}{\gamma-1}}} \; , \tag{4.1}$$

where C_d is the discharge coefficient, ψ the flow coefficient and γ the heat capacity ratio of the gas at higher pressure

$$\gamma = \frac{C_p}{C_V} \; . \tag{4.2}$$

The outflow is called critical or choked when

$$\frac{p_1}{p_2} \geq (\frac{\gamma + 1}{2})^{\frac{\gamma}{\gamma-1}} \; . \tag{4.3}$$

In this case,

$$\psi = 1 \; . \tag{4.4}$$

For subcritical flow, one has:

$$\psi = \sqrt{\frac{2}{\gamma - 1} (\frac{\gamma + 1}{2})^{\frac{\gamma+1}{\gamma-1}} (\frac{p_2}{p_1})^{\frac{2}{\gamma}} (1 - (\frac{p_2}{p_1})^{\frac{\gamma-1}{\gamma}})} \; . \tag{4.5}$$

Typical values for the discharge coefficient range from 0.6 to 0.99. However, in this thesis, the simple orifice is a model for an orifice followed by a piping that adds additional flow resistance and good results have been achieved with a C_d value of 0.15. More specifically,

Die approbierte gedruckte Originalversion dieser Diplomarbeit ist an der TU Wien Bibliothek verfügbar
The approved original version of this thesis is available in print at TU Wien Bibliothek.
TU Bibliothek Your knowledge hub WIEN

the value of C_d was fitted to the results of one experiment and then used for the second experiment to verify whether the fitted value generalizes to the other case of interest. Formula (4.1) can be derived from the first law of thermodynamics for a quasi-static flow process as shown in [19].

4.2 Water outflow

A simple expression for the flow of water through an orifice or through a nozzle can be derived using the Bernoulli equation, as shown for a similar example in [4]. The Bernoulli equation relates the pressure and flow velocity at different points in a system:

$$p_1 + \frac{1}{2}\rho v_1^2 = p_2 + \frac{1}{2}\rho v_2^2 \tag{4.6}$$

Now, assuming that on one side the flow is very slow, which is a reasonable assumption if one side is a pipe and the other is a large water vessel in case of the orifice or the environment in case of the nozzle, the velocity on that side can be neglected. Then, one gets the following expression for the flow:

$$q = vA \tag{4.7}$$

$$= A\sqrt{\frac{2}{\rho}(p_1 - p_2)} \tag{4.8}$$

$$= k_v\sqrt{p_1 - p_2}\ . \tag{4.9}$$

Because the neglected velocities will not be exactly zero and the flow might not be laminar this expression will not be exact, and an effective k_v value was fitted to match the results for one experiment and used again for the second to test whether the fitted value can be generally applied.

4.3 Darcy-Weisbach Equation

Pipe lengths of 100 meters, or even more, are often used between the water vessel and the nozzle heads, leading to a significant pressure drop between the two. This pressure loss is estimated using the Darcy-Weisbach equation expressed in terms of the friction factor λ. Both the equation and different ways of approximating the friction factor are explained in detail in [20]. Here, it should be mentioned that the equation and the different formulas for the friction factor are empirically found relations. For this thesis, the Darcy-Weisbach equation for a pipe of length L with diameter d and a fluid with density ρ and velocity v was used in the form

$$\Delta p = \lambda\frac{L\rho v^2}{2d}\ . \tag{4.10}$$

Die approbierte gedruckte Originalversion dieser Diplomarbeit ist an der TU Wien Bibliothek verfügbar
The approved original version of this thesis is available in print at TU Wien Bibliothek.

Furthermore, one has to consider that corners in the pipe add additional flow resistance and, thus, enhance the pressure loss. This can be approximated by modifying the length to be the sum of the true pipe length L_0 plus an equivalent length L_c for each corner:

$$L = L_0 + N_c \, L_c \tag{4.11}$$

For perpendicular corners in a pipe with nine millimeter inner diameter and twelve millimeter outer diameter, the length equivalent was taken from [21] which refers to [22] as:

$$L_c = 0.31 \text{ m} \, . \tag{4.12}$$

For laminar flow, which is typically assumed for Reynolds numbers

$$\mathrm{Re} = \frac{vl}{\nu} < 2300 \, , \tag{4.13}$$

with kinematic viscosity ν and characteristic lengths of the body in which the fluid flows l, the friction factor can be approximated by

$$\lambda \cong \frac{64}{\mathrm{Re}} \, . \tag{4.14}$$

For higher Reynolds numbers the implicit Colebrook-White equation

$$\frac{1}{\sqrt{\lambda}} = -2 \log_{10}\left(\frac{K}{3.7} + \frac{2.51}{\mathrm{Re}\sqrt{\lambda}}\right) \tag{4.15}$$

with K being the ratio of the pipes equivalent sandwall roughness by its inner diameter was used, and solved iteratively for λ. For the real gas model ν was calculated with the method presented in [23], that was already implemented in CoolProp. For the ideal gas and van der Waals gas models, the Andrade equation, as given in [24],

$$\nu = \frac{a}{\rho} \, e^{\frac{b}{RT}} \tag{4.16}$$

was used. The parameters a and b were fitted using least squares with viscosity data from [4]. The resulting parameters were $a = 9.815 \cdot 10^{-7}$ Pa $\cdot$ s and $b = 16983.17$ mol $\cdot$ J^{-1}.

Die approbierte gedruckte Originalversion dieser Diplomarbeit ist an der TU Wien Bibliothek verfügbar
The approved original version of this thesis is available in print at TU Wien Bibliothek.
TU Bibliothek Your knowledge hub WIEN

5 Experiment

In the following chapter the experimental setup for both GPP experiments is described in Section 5.1. First, the setup of the firefighting is explained. This is followed by a description of the measurement devices and measurement points. In Section 5.2 the results of the two experiments with argon are displayed. For both experiments, the pressure at the different measurements is plotted first over the whole duration of the spraying process and then over the first 30 seconds for a better resolution of the initial expansion process. Then the measured temperature data throughout the spraying process is displayed.

5.1 Experimental Setup

5.1.1 Fire Suppression System Components

The argon gas was stored in vessels with a volume of 50 liters. The vessels are made of steel with black paint on the outside. Although they are approved for pressures up to 300 bar, systems are typically built with up to about 200 bar pressure and temperatures between -25 to +65 °C. They have a diameter of 229 millimeters and a total length of 1405 millimeters. These gas vessels were connected through a trigger valve and approximately one meter of piping with an inner diameter of nine millimeters to another steel vessel containing water. This vessel had a plastic coating on the inside and was approved for ambient temperatures in the range from +5 to +55°C. It had a volume of 67.5 liters with a length of 1430 millimeters and a diameter of 267 millimeters. Both vessels can be seen in Figure 5.1.

Through a riser pipe and a one-meter-long hose, the water in the vessel had access to a 96-meter-long piping system with 34 prependicular corners and an inner diameter of nine millimeters. The piping system can be seen in Figure 5.2. At the end of this piping system, a stainless steel DKO-R01 nozzle head as seen in Figure 5.3 was attached. It has a k-factor of 0.4875 liters per minute and bar and is a commonly used nozzle head in rail vehicles.

Die approbierte gedruckte Originalversion dieser Diplomarbeit ist an der TU Wien Bibliothek verfügbar
The approved original version of this thesis is available in print at TU Wien Bibliothek.
TU Bibliothek Your knowledge hub WIEN

Figure 5.1: Gas vessel (black) and water vessel (blue) mounted in a GPP fixture. The three blue cylinders connected to the gray cables are HySense PR 400 piezoelectrive pressure sensors.

Figure 5.2: Piping system to simulate a real life situation where the water has to flow through long pipes to reach the nozzle head.

Die approbierte gedruckte Originalversion dieser Diplomarbeit ist an der TU Wien Bibliothek verfügbar
The approved original version of this thesis is available in print at TU Wien Bibliothek.
TU Bibliothek Your knowledge hub WIEN

Figure 5.3: A DKO-R01 nozzle head as is typically used in rail vehicles. It is built in with the nozzles facing downwards.

Die approbierte gedruckte Originalversion dieser Diplomarbeit ist an der TU Wien Bibliothek verfügbar
The approved original version of this thesis is available in print at TU Wien Bibliothek.
TU Bibliothek Your knowledge hub WIEN

5.1.2 Measurement devices

The most important quantity for a GPP is the pressure. To measure the pressure, piezoresistive pressure sensors were used. More specifically, five Hydrotechnik HySense PR 400 sensors were exploited to measure pressure at five different points in the system:

1. The gas vessel
2. The pipe right after the trigger valve
3. The pipe right after the water vessel
4. The pipe right after the hose
5. At the nozzle head.

The first three can also be seen in Figure 5.1. The measurement after the hose was made to ensure that there is no large pressure drop due to the hose itself. Since there was no significant pressure drop, this data set was not used any further. Similarly, the measurement right after the trigger valve yielded nearly identical pressures as in the gas vessel and was thus also not used. As water is hardly compressible, the pressure immediately after the water vessel was assumed to be identical to the pressure in the water vessel. The pressure loss through the riser pipe is negligible. Typical errors of these sensors are below 0.25%. The pressures were recorded using a MultiSystem 4070 from Hydrotechnik, which automatically recognizes connected sensors and sets relevant parameters, such as the measurement range. The device used can be seen in Figure 5.4.

Furthermore, the temperature of the gas vessel vessel was measured using type K thermocouples, which were attached to the vessel wall using thermally insulating self-adhesive aluminum foil at three points of the gas vessel, one at the bottom, one in the middle and one at the top, as it can be seen in Figure 5.5.

5.2 Experimental Results

Due to the Joule-Thomson effect, the argon and gas vessels themselves warmed during the filling process. In a real system, the vessel and the gas have cooled to ambient temperature when triggered. Thus, the vessels were filled a few days before the experiment to ensure ambient temperature. Furthermore, due to safety regulation, the set-up was built and triggered by trained personnel in the AQUASYS laboratory at the presence and under the indications of the author. The two different pressures used for the experiments are chosen to represent a wide range of actually used working pressures to assess each model performance for different starting conditions.

Die approbierte gedruckte Originalversion dieser Diplomarbeit ist an der TU Wien Bibliothek verfügbar
The approved original version of this thesis is available in print at TU Wien Bibliothek.
TU Bibliothek Your knowledge hub WIEN

Figure 5.4: Multisystem 4070 used for recording the pressure measurement values. The gray box on the right is the manual trigger for the trigger valve to open. At the time when this picture was taken, the valve was still closed, as can be seen on the multisystem where the gas vessel pressure is at the initial pressure of 202 bar while all other pressures are zero.

Figure 5.6 sketches the expected temporal development of the pressure at the different measurement points in the system. In the initial phase (i), the gas expands into the water vessel and presses the water into the piping system. The water outflow is not yet limited by the spray head at this time. This leads to a very rapid expansion and a rapid pressure drop in the gas vessel and a pressure increase in the water vessel. Phase (ii) starts when the water in the piping system reaches the nozzle head. In this phase, the volume outflow is restricted by the nozzle head leading to a slower gas expansion and smaller pressure changes. The flow resistance in the piping system causes a pressure drop between the water vessel and the nozzle head. After some time, the water level in the water vessel will drop below the entrance of the riser pipe. In this final phase (iii) the gas expands

Die approbierte gedruckte Originalversion dieser Diplomarbeit ist an der TU Wien Bibliothek verfügbar
The approved original version of this thesis is available in print at TU Wien Bibliothek.
TU Bibliothek Your knowledge hub WIEN

Figure 5.5: Type K thermocouples were attached to the gas vessel at three different positions using self-adhesive and thermally insulating aluminum foil.

into the piping system. The pressure drop of the gas in the piping system is smaller than the pressure drop of the water. This leads to a convergence of the pressure curves in the final phase until the gas reaches the nozzle head and the spraying ends. Here, it should be mentioned that phases (i) and (iii) are typically much shorter than phase (ii). Their duration has been greatly exaggerated in Figure 5.6 for a better visualization.

Die approbierte gedruckte Originalversion dieser Diplomarbeit ist an der TU Wien Bibliothek verfügbar
The approved original version of this thesis is available in print at TU Wien Bibliothek.

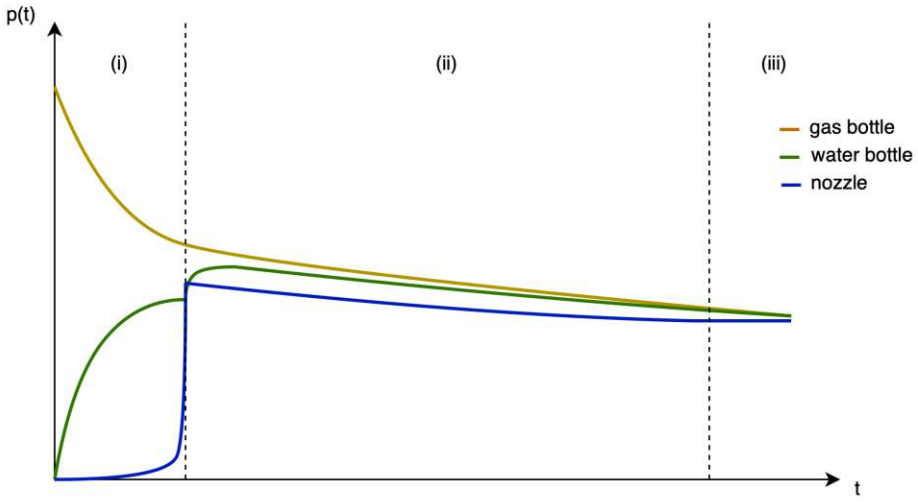

Figure 5.6: Schematic visualization of the form of the expected temporal pressure development at the different measurement points in the system.

5.2.1 152 Bar Experiment

For the first experiment, the gas vessel was filled with argon up to a pressure of about 152 bar. The water vessel was filled with about 60.8 liters of water, the rest of the volume was filled with air. The measured pressure at the three measurement points described above can be seen in Figure 5.7. The spraying process stopped after 810 seconds. Due to the fact that the riser pipe does not reach all the way to the bottom, about 1.7 liters of water eventually remained in the water vessel.

The temporal development of the pressure at the measurement points follows the three-phase progression explained before. In the first few seconds, the initial gas flow from the gas vessel to the water vessel is large due to the high difference in pressure of these systems. Therefore, fast expansions and pressure changes occur. In order to better visualize this initial pressurization, Figure 5.8 shows only the first 30 seconds of Figure 5.7. One sees that the pressure in the gas vessel (yellow) decreases rapidly while the pressure in the water vessel (green) increases rapidly. The pressure at the nozzle (blue) remains quite low as the water is pressed through the piping system and compresses the remaining air until the water reaches the nozzle head and the pressure rapidly increases after about eight seconds. The large oscillations of the pressure at the nozzle appear at exactly the same time when the water first reaches the nozzle head but get damped within a few seconds. The exact moment when the spraying begins can also be seen in the pressure of the water vessel. In fact, after activation, the water is pumped into the piping system and

Die approbierte gedruckte Originalversion dieser Diplomarbeit ist an der TU Wien Bibliothek verfügbar
The approved original version of this thesis is available in print at TU Wien Bibliothek.
TU Bibliothek Your knowledge hub WIEN

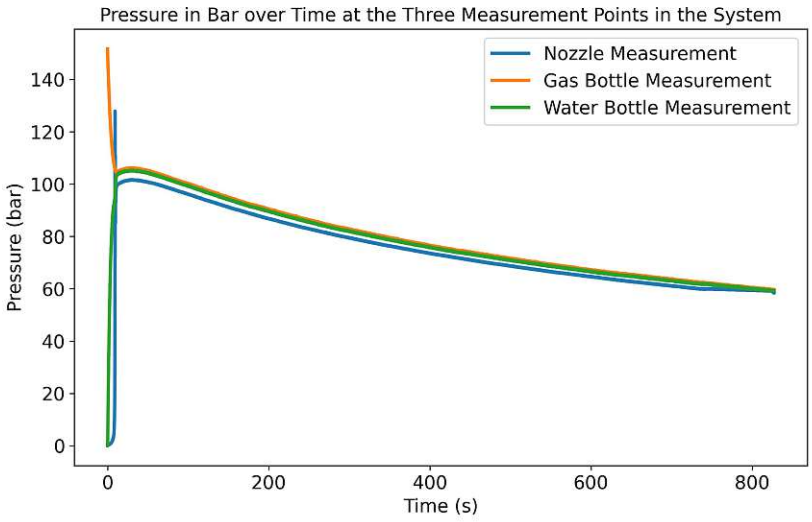

Figure 5.7: Pressure in bar over time for the whole spraying time in the 152 bar experiment.

the initial flow resistance is smaller than the flow resistance when the water has reached the nozzle head. Thus, when the water first reaches the nozzle head, the flow resistance suddenly increases. This leads to a jump in the pressure being transferred all the way back to the water vessel. The sudden increase in pressure can be seen in Figure 5.8 and aligns perfectly with the sudden increase in pressure at the nozzle head. The pressure loss between the gas and the water vessel becomes negligible after about fifteen seconds. However, a significant pressure loss remains between the water vessel and the nozzle head. As expected, because of the Joule-Thomson effect, through expansion the temperature of the gas declines. However, a direct measurement of gas temperature is not possible, so the vessel wall temperatures were measured with thermocouples at three evenly spaced positions of the vessel: one at the bottom (blue), one in the middle (yellow), and one at the top (green). Figure 5.9 shows the temperature measured at all positions of the vessel. Since only one overall temperature is calculated in the simulation, the average temperature (dashed line) is also plotted. The decline is strongest at the beginning when the gas expands faster and flattens out as the expansion slows down and the ambient air provides more energy because the heat convection depends linearly on the temperature difference between the vessel wall and the ambient air, as is explained in Section 3.6.

Die approbierte gedruckte Originalversion dieser Diplomarbeit ist an der TU Wien Bibliothek verfügbar
The approved original version of this thesis is available in print at TU Wien Bibliothek.

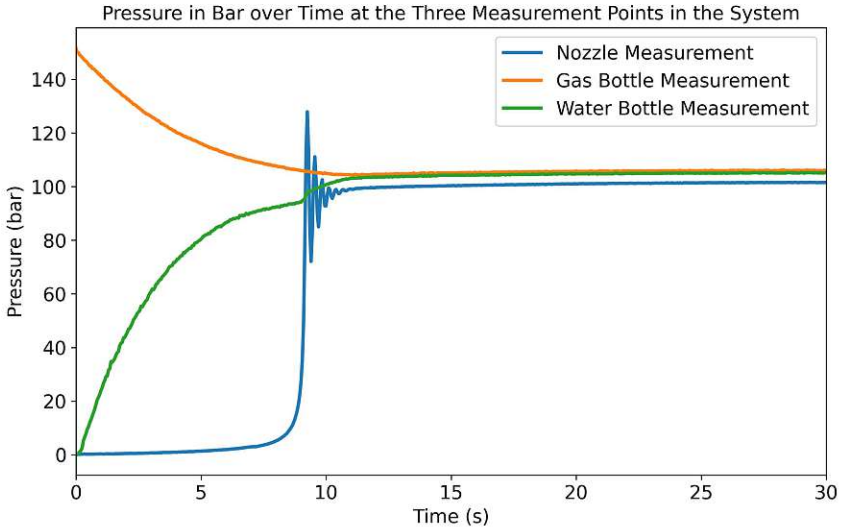

Figure 5.8: Pressure in bar over time for the approximately first 30 seconds in the 152 bar experiment.

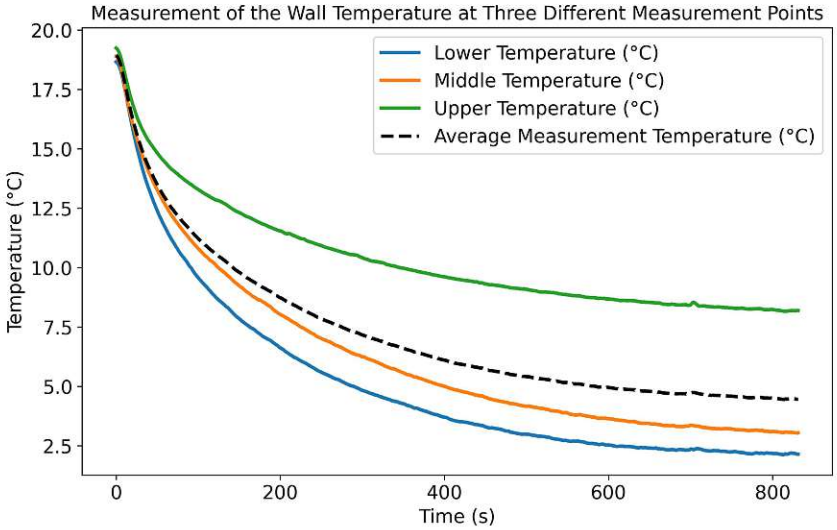

Figure 5.9: Gas vessel wall temperature over time during the spraying process for the 152 bar experiment.

Die approbierte gedruckte Originalversion dieser Diplomarbeit ist an der TU Wien Bibliothek verfügbar
The approved original version of this thesis is available in print at TU Wien Bibliothek.

5.2.2 202 Bar Experiment

For the second experiment, the gas vessel was filled with argon to a pressure of 202 bar. The water vessel was filled with 61 liters of water. The pressures at the three measurement points as a function of the time can be seen in Figure 5.10. Due to the higher operating pressure over time, water is sprayed faster through the nozzle head, and thus the water vessel empties faster, in this case after about 730 seconds (compared to over 800 in the 152 bar experiment).

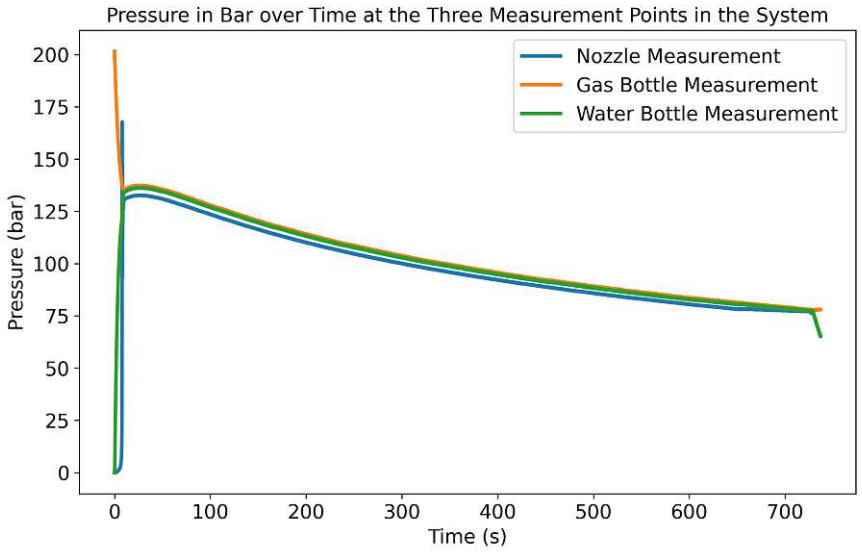

Figure 5.10: Pressure in bar over time for the whole spraying time in the 202 bar experiment.

As done before, Figure 5.11 shows the first 30 seconds after the trigger. As the initial pressure is higher, the water is pressed faster through the piping system. Thus, the time between the trigger and the start of spraying is shorter.

Similarly to the initial expansion, the temporal decline is also faster, as clearly visualized in Figure 5.12. Temperatures below the freezing point were measured at the base of the vessel, and this phenomenon was also evident to the naked eye, as water from the ambient air condensed on the vessel's surface.

Die approbierte gedruckte Originalversion dieser Diplomarbeit ist an der TU Wien Bibliothek verfügbar
The approved original version of this thesis is available in print at TU Wien Bibliothek.

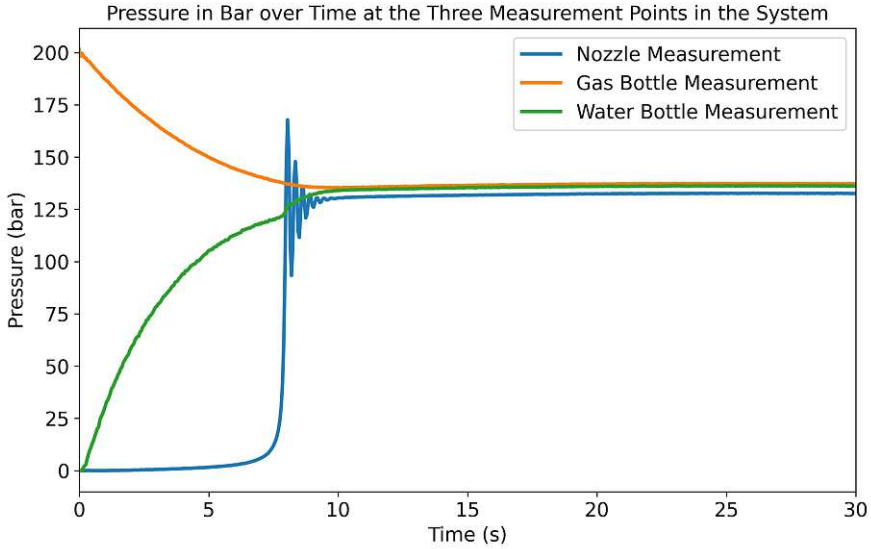

Figure 5.11: Pressure in bar over time for the approximately first 30 seconds in the 202 bar experiment.

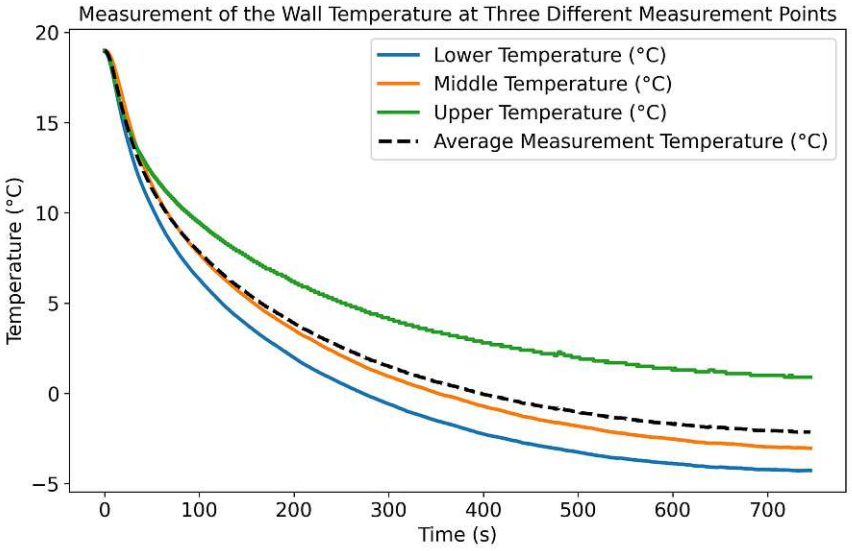

Figure 5.12: Gas vessel wall temperature over time during the spraying process for the 202 bar experiment.

Die approbierte gedruckte Originalversion dieser Diplomarbeit ist an der TU Wien Bibliothek verfügbar
The approved original version of this thesis is available in print at TU Wien Bibliothek.
TU Bibliothek Your knowledge hub WIEN

6 Computational Methods

This chapter concisely introduces the Euler method following [25] in Section 6.1. A comparison with CFD methods and an analysis of why Euler might be better suited for the scope of this thesis work is provided in Section 6.2.

6.1 Euler's Method

As the system of differential equations given in this thesis cannot be solved analytically, numerical methods must be used.

As a starting point, we consider the Taylor expansion for a differential equation

$$\frac{dy}{dt} = f(y,t) \tag{6.1}$$

at the discretized timestep t_{i+1}, which is given by

$$y(t_{i+1}) = y(t_i) + y'(t_i)(t_{i+1} - t_i) + \mathcal{O}((t_{i+1} - t_i)^2) \tag{6.2}$$
$$\approx y(t_i) + f(y(t_i), t_i)\Delta t \ . \tag{6.3}$$

Now, with a known starting value, one can formulate the explicit Euler algorithm:

$$y_0 = y(t_0) \ , \tag{6.4}$$
$$y_{i+1} = y_i + f(y_i, t_i)\Delta t \ . \tag{6.5}$$

The error of each individual time step for this method is $\mathcal{O}(\Delta t^2)$. However, errors from previous steps influence the starting values of later steps, so that errors might start to accumulate. A heuristic approximation can be obtained taking into account that local step errors decrease with Δt^2 while the number of steps increases with Δt. Thus, the global error should decrease with Δt. For Lipschitz continuous derivatives f this can be proven, as it is done, for example, in [25]. Thus, the explicit Euler method is considered to be a first-order method.

6.2 Comparison with CFD

Computational Fluid Dynamics (CFD) is a widely used and probably the most accurate method to solve fluid mechanics problems. It works by defining the relevant geometries

Die approbierte gedruckte Originalversion dieser Diplomarbeit ist an der TU Wien Bibliothek verfügbar
The approved original version of this thesis is available in print at TU Wien Bibliothek.

using computer-aided design. The geometry is then divided into a fine mesh of finite volumes or elements. The initial values and boundary conditions must then be defined. If all these steps are performed with reasonable accuracy, very good results can be obtained. However, there are also some disadvantages. Inaccuracies in the definition of the geometry can lead to significant deviations in the result. Furthermore, creating a good mesh is a complex task. Many packages that would make initialization easier are commercial and very expensive. With open source packages, the definition of a system of equations is usually very complicated. Finally, the computational effort for a fine mesh is very high. This is also the main reason why the Euler method was chosen for this Master thesis work. If the Euler method can achieve results of high enough accuracy, the computational effort of CFD methods would be, in fact, unnecessary.

Die approbierte gedruckte Originalversion dieser Diplomarbeit ist an der TU Wien Bibliothek verfügbar
The approved original version of this thesis is available in print at TU Wien Bibliothek.

7 Modeling of the System

In this chapter the simplifications made to model the fire extinguishing system are explained in Section 7.1. This is followed by the illustration of the calculations for updating the state for each thermodynamical subsystem in Sections 7.2, 7.3 and 7.4. Finally, the complete calculation algorithm is shown in Section 7.5.

7.1 Simplification of the system

We start by noting that, since the pressure loss due to flow resistance between the gas vessel and the water vessel was negligible, it was not included in the calculation. Within this assumption, the system was modeled as follows. The complex geometry of the gas and water vessels was schematized to a cylinder geometry and their connection was simplified to be an orifice. Even at the starting time, the water vessel is not fully filled with water, but there is some residual gas at the top. Although this residual gas is air at the beginning, the amount of argon increases rapidly and thus the second gas was also treated with the equations of state fitted for argon. A riser pipe goes down inside the water vessel and connects the water to a long pipe with multiple 90 degree corners and finally ends in a nozzle head through which the water is sprayed into the environment. A sketch of this model can be seen in Figure 7.1.

The whole system was divided into three thermodynamical subsystems. First, the argon gas in the gas vessel. It delivers the operating pressure of the system by expanding through the orifice, in this way losing mass and reducing its density. Through the process of expansion, it also decreases its temperature. Heat is transferred between the gas and the environment through the wall of the vessel. Calculations for a single gas vessel that discharges into the environment were already implemented in the Hyddown Python package [11] and were taken as a theoretical and code basis for simulation in this thesis.

Then, there is the second gas, which is air at the beginning, but quickly is mostly consisting of argon too. It gets additional mass because of the mass flow through the orifice. It is in direct contact with the water and presses it into the riser pipe to the nozzle head. It exchanges heat with the part of the vessel wall it is in contact with and with the water itself. Because of the high pressure, it also compresses the water a little.

Finally, also the water in the water vessel is treated as a subsystem itself. It loses mass by flowing into the riser pipe and exchanges heat with the gas and the wall surface with which it is in contact. Because the riser pipe does not fully reach the bottom of the vessel, a water amount the size of about two percent of the water vessel volume typically remains in the water vessel and is not sprayed into the environment. In the following, to distinguish which subsystem a specific thermodynamic variable, such as pressure, refers

Die approbierte gedruckte Originalversion dieser Diplomarbeit ist an der TU Wien Bibliothek verfügbar
The approved original version of this thesis is available in print at TU Wien Bibliothek.
TU Bibliothek Your knowledge hub WIEN

to, variables relating to the first gas are assigned a superscript $^{(1)}$, those relating to the second gas are assigned $^{(2)}$ and those relating to water are assigned $^{(W)}$. If quantities refer to the vessel walls, their superscript is $^{(w1)}$ or $^{(w2)}$, respectively, and finally the values that refer to the nozzle head are assigned the superscript $^{(n)}$.

For the ideal gas model and the van der Waals gas model the molar weight of argon was needed in the calculations. The used value of

$$M = 39.948 \frac{\mathrm{g}}{\mathrm{mol}} \tag{7.1}$$

was taken from [26].

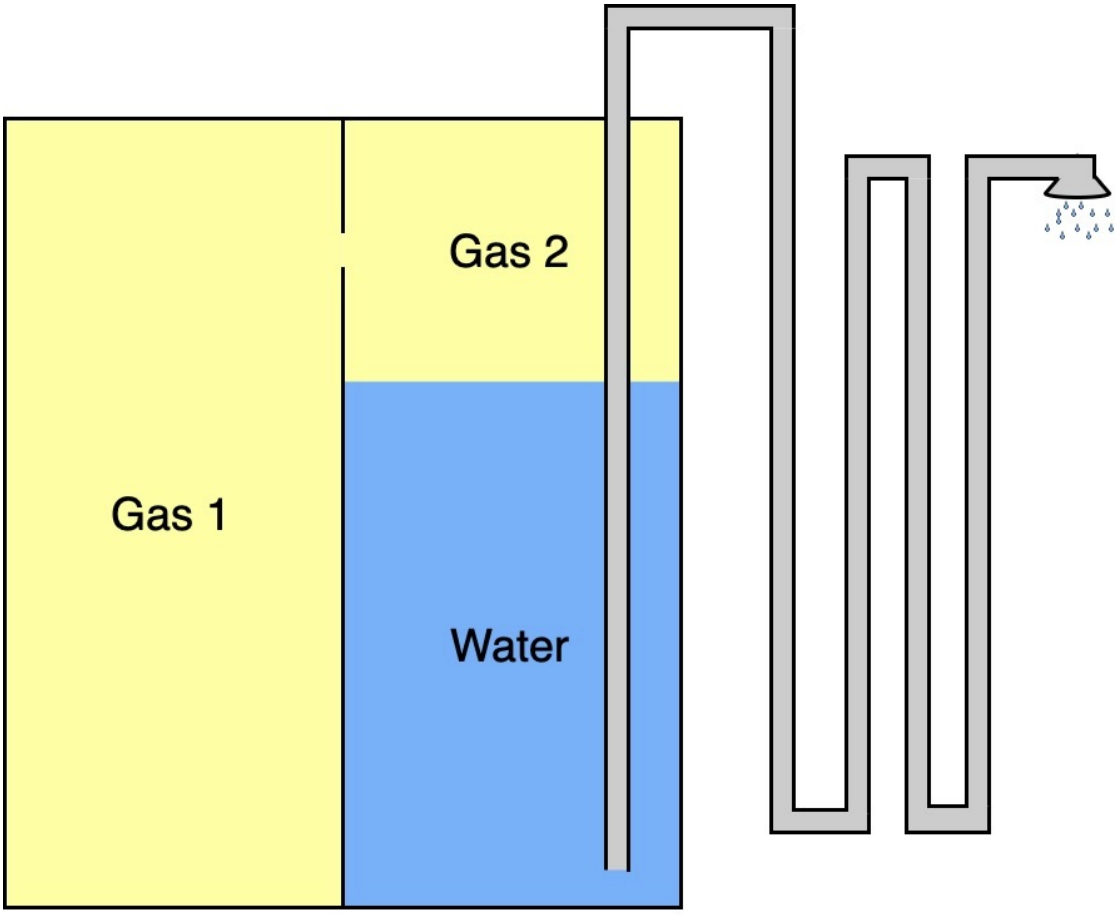

Figure 7.1: A sketch of the model used to describe the actual (more complicated) fire extinguishing system.

Die approbierte gedruckte Originalversion dieser Diplomarbeit ist an der TU Wien Bibliothek verfügbar
The approved original version of this thesis is available in print at TU Wien Bibliothek.
TU Bibliothek Your knowledge hub WIEN

7.2 Gas 1

As mentioned before, the calculations for a single discharging gas vessel can be found in [11]. Assuming that for some prior time t_i the state of the gas is known, as well as the temperature of the gas vessel wall, the state of the gas at t_{i+1} can be calculated with the methods presented in the Chapters 3, 4, and 6. In particular, the mass flow rate can be computed with Equation (4.1). Then, the new total mass of the gas can be obtained by

$$m_{i+1}^{(1)} = m_i^{(1)} - \Delta m_i \approx m_i^{(1)} - \dot{m}_i \ \Delta t \ , \tag{7.2}$$

and the new density by

$$\rho_{i+1}^{(1)} = \frac{m_{i+1}^{(1)}}{V^{(1)}} \ . \tag{7.3}$$

The gas loses inner energy by work. The remaining part of the gas expands by pushing the flowing gas out of the gas vessel. In addition, it loses the inner energy of the gas that leaves through the mass flow. Furthermore, heat exchange with the vessel wall must be taken into account. This leads to a new inner energy value, given by

$$\begin{aligned} U_{i+1}^{(1)} &= U_i^{(1)} + \delta Q_i^{(1)} + \delta W_i^{(1)} - dm_i \ \frac{U_i^{(1)}}{m_i^{(1)}} && (7.4)\\ &\approx U_i^{(1)} + \delta Q_i^{(1)} - p_i^{(1)}(\Delta m_i \frac{V^{(1)}}{m_i^{(1)}}) - \Delta m_i \ u_i^{(1)} && (7.5)\\ &= U_i^{(1)} + \delta Q_i^{(1)} - \Delta m_i (u_i^{(1)} + p_i^{(1)} \ v_i^{(1)}) && (7.6)\\ &= U_i^{(1)} + \delta Q_i^{(1)} - \Delta m_i \ h_i^{(1)} \ . && (7.7) \end{aligned}$$

with mass-specific enthalpy h_i. The heat exchange is estimated by means of the following equation:

$$\delta Q_i^{(1)} \approx \ \kappa_i^{(1,w1)} (T_i^{(w1)} - T_i^{(1)}) \ A^{(1)} \ \Delta t \ , \tag{7.8}$$

where A is the inner surface of the vessel. The heat transfer coefficient $\kappa_i^{(1,w1)}$ is, as explained in Section 3.6, explicitly calculated for the real gas model and approximated by the value 100 $\frac{\mathrm{W}}{\mathrm{m^2K}}$ based on the range of values given in [14] for the ideal gas and the van der Waals gas. The vessel wall also exchanges heat with the environment. The heat that flows from the environment into the vessel wall is approximated by

$$\delta Q_i^{(w1)} = \kappa^{(w1,\mathrm{amb})} \ (T^{\mathrm{amb}} - T_i^{(w1)}) \ \Delta t \ , \tag{7.9}$$

Die approbierte gedruckte Originalversion dieser Diplomarbeit ist an der TU Wien Bibliothek verfügbar
The approved original version of this thesis is available in print at TU Wien Bibliothek.

where the value of $\kappa^{(w1,\mathrm{amb})}$ is approximated by 11 $\frac{\mathrm{W}}{\mathrm{m^2K}}$, which is as well an approximation value based on [14] as explained in Section 3.6. The updated wall temperature can then be calculated by

$$T_{i+1}^{(w1)} = T_i^{(w1)} + \frac{(\delta Q_i^{(w1)} - \delta Q_i^{(1)})}{c_p \; m^{(w1)}} \; . \tag{7.10}$$

In particular, in the case of the ideal gas model the temperature of the gas itself can be explicitly obtained from the energy-temperature relation, which for a one-atomic gas reads

$$T_{i+1}^{(1)} = \frac{2 \; U_{i+1}^{(1)}}{3 \; k_B \; N_{i+1}^{(1)}} = \frac{2 \; U_{i+1}^{(1)} \; M}{3 \; k_B \; m_{i+1}^{(1)}} \; , \tag{7.11}$$

with M being, here, the atomic weight of argon. In case of the van der Waals gas, the dependence of the inner energy on the volume has to be taken into account. This leads to a slightly more complicated expression:

$$T_{i+1}^{(1)} = \frac{2 \; (U_{i+1}^{(1)} + \frac{a N_{i+1}^{2(1)}}{V^{(1)}})}{3 \; k_B \; N_{i+1}^{(1)}} \tag{7.12}$$

$$= \frac{2 \; U_{i+1}^{(1)} \; V^{(1)} + a \; N_{i+1}^{2(1)}}{3 \; k_B \; N_{i+1}^{(1)} \; V^{(1)}} \tag{7.13}$$

$$= \frac{2 \; U_{i+1}^{(1)} \; V^{(1)} \; M^2 + a \; m_{i+1}^{2(1)}}{3 \; k_B \; m_{i+1}^{(1)} \; V^{(1)} \; M} \; . \tag{7.14}$$

In case of the real gas model, the temperature can instead be obtained from the EOS. Eventually, the corresponding pressure can be computed from the respective EOS for all models:

$$p_{i+1}^{(1)} = \mathrm{EOS}(\rho_{i+1}^{(1)}, T_{i+1}^{(1)}) \; . \tag{7.15}$$

7.3 Gas 2

As the second gas shares a vessel with the water, the corresponding calculations are more complex than for the first gas. Similarly as before, the updated mass of the gas can be calculated with

$$m_{i+1}^{(2)} = m_i^{(2)} + \Delta m_i \approx m_i^{(2)} + \dot{m}_i \; \Delta t \; , \tag{7.16}$$

Die approbierte gedruckte Originalversion dieser Diplomarbeit ist an der TU Wien Bibliothek verfügbar
The approved original version of this thesis is available in print at TU Wien Bibliothek.
TU Bibliothek Your knowledge hub WIEN

and the updated density with

$$\rho_{i+1}^{(2)} = \frac{m_{i+1}^{(2)}}{V_{i+1}^{(2)}} \ . \tag{7.17}$$

But now, the volume is no longer constant as it was for the first gas. It changes through compression of the water and through flow of water into the riser pipe:

$$\Delta V_i = \Delta V_i^c + \Delta V_i^f \ . \tag{7.18}$$

The volume change for the gas through compression was estimated by the negative change of volume of the water

$$\Delta V_i^c = V_{i-1}^{(W)} - V_i^{(W)} \tag{7.19}$$

$$= \frac{m_i^{(W)}}{\rho_{i-1}^{(W)}} - \frac{m_i^{(W)}}{\rho_i^{(W)}} \tag{7.20}$$

$$= m_i^{(W)} \frac{\rho_i^{(W)} - \rho_{i-1}^{(W)}}{\rho_i^{(W)} \ \rho_{i-1}^{(W)}} \ , \tag{7.21}$$

where $m_i^{(W)}$ and $\rho_i^{(W)}$ are the mass and density of water. Note that for the ideal gas model and the van der Waals gas model, as already mentioned in Section 3.6, no tabulated data was accessible. Therefore, the water was assumed to be incompressible:

$$\Delta V_i^c = 0 \ . \tag{7.22}$$

The flow volume change depends on the state of the whole system. In particular, it depends on whether the water has already reached the nozzle head or not. In both cases, the volume flow rate can be calculated by Equation (4.9), here given with pressures in bars for an easier implementation:

$$q_i = k\sqrt{p_1 - p_2}, \tag{7.23}$$

with a different value of k for the two cases. Specifically, until the water has reached the nozzle head, k is given by

$$k_1 = 0.097 \frac{\mathrm{l}}{\mathrm{s}\sqrt{\mathrm{bar}}} \tag{7.24}$$

with l being liters and s seconds. In this case p_1 is the pressure in the water vessel and p_2 is estimated by the ambient air pressure of 1 bar. If the water has reached the nozzle

Die approbierte gedruckte Originalversion dieser Diplomarbeit ist an der TU Wien Bibliothek verfügbar
The approved original version of this thesis is available in print at TU Wien Bibliothek.
TU Bibliothek Your knowledge hub WIEN

head instead, the flow through the nozzle head should also be considered, yielding

$$k_2 = 0.008125 \frac{\mathrm{l}}{\mathrm{s}\sqrt{\mathrm{bar}}}, \tag{7.25}$$

where p_1 is the pressure at the nozzle head and p_2 again the ambient air pressure of 1 bar. To obtain the pressure at the nozzle head, a minimization algorithm was developed. The pressure loss was calculated with the method presented in Section 4.3. However, the Darcy-Weisbach equation uses the flow velocity v explicitly. Furthermore, the velocity is needed in the calculation of the friction factor λ. The velocity can then be calculated as the ratio of the flow Q_i divided by the cross-section area of the pipes A:

$$v_i = \frac{q_i}{A} \tag{7.26}$$

$$< = \frac{k_2}{A} \sqrt{p_i^{(n)} - p^{\mathrm{amb}}} \tag{7.27}$$

$$= \frac{k_2}{A} \sqrt{p_i^{(W)} - \Delta p_i - p^{\mathrm{amb}}} \tag{7.28}$$

Thus, the velocity itself depends on the pressure loss. This means that the Darcy-Weisbach equation becomes, in this case, an implicit equation to be solves self-consistently. It was then solved in each iteration step by minimizing a function

$$f(\Delta p_i) = (\Delta p_i - \Delta p_i(v_i(\Delta p_i))^2 \tag{7.29}$$

using the SciPy [27] implementation of the Nelder-Mead algorithm as shown in [28]. An important detail to be emphasized, once more, is that not all the water in the water vessel reaches the nozzle head, as a residual water mass m_r stays in the water vessel. This is because the riser pipe does not reach the bottom of the vessel. If the water level in the water vessel was below the entrance of the riser pipe, the gas would no longer push more water into the piping system but would expand into the piping system itself. A calculation of the pressure loss of the gas flowing through the piping system would require an elaborate approach using the Navier-Stokes equations for compressible flow as given in [29] and was neglected for simplicity. However, in the case of the gas expanding into the piping system, the distance that water travels through the piping system decreases. Assuming that the corners are distributed equidistantly through the piping system, the effective length for the pressure loss calculation decreases. The updated length is given by

$$L_{i+1} = L_i - L \frac{\Delta V_i^f}{r_p^2 \pi L_0} \ , \tag{7.30}$$

Die approbierte gedruckte Originalversion dieser Diplomarbeit ist an der TU Wien Bibliothek verfügbar
The approved original version of this thesis is available in print at TU Wien Bibliothek.
TU Bibliothek Your knowledge hub WIEN

where L is the effective length, that includes the flow resistance added by the corners, L_0 is the actual length and r_p is the pipe radius. Mathematically, this means that the volume change was subtracted from the piping systems volume and added to the water vessel volume. Finally, the flow-induced volume change has been approximated by

$$\Delta V_i^f = q_i \ \Delta t \ . \tag{7.31}$$

The change in volume indicates that the gas applies work to the water by pressing it through the piping system. This introduces an additional term in the formula to update the inner energy:

$$U_{i+1}^{(2)} = U_i^{(2)} + \delta Q_i^{(2)} + \Delta m_i \ h_i^{(1)} - p_i^{(2)} \ \Delta V_i^{(2)} \tag{7.32}$$

Note that, because of energy conservation, the energy deducted from the first gas by mass flow must be added to the second gas. The heat flow is calculated similarly to the case of gas 1, but now the inner surface also changes with every step, and additional heat exchange with the water should be considered:

$$\delta Q_i^{(2)} = \delta Q_i^{(2-w2)} + \delta Q_i^{(2-W)} \tag{7.33}$$

$$\approx \ \kappa_i^{(2,w2)}(T_i^{(w2)} - T_i^{(2)}) \ A_i^{(2)} \ \Delta t + \ \kappa_i^{(2,W)}(T_i^{(W)} - T_i^{(2)}) \ r^2\pi \ \Delta t \ , \tag{7.34}$$

where r is the radius of the vessel and the area is updated in each time step by

$$A_{i+1}^{(2)} = A_i^{(2)} + \frac{\Delta V_i}{r^2\pi} \ . \tag{7.35}$$

With the new ρ_{i+1} and U_{i+1} all other quantities can be calculated similarly to the first gas. However, the vessel wall interacts now not only with the gas but also with the water. Thus, to update the temperature of the vessel wall, the heat exchange between water and vessel wall must be calculated first.

7.4 Water

Because the water is in direct contact with the second gas and the pressure propagates with the speed of sound, the new water pressure in a new time step is approximated by the pressure in the second gas. Using the volume flow expression of Equation (7.31), the mass flow can be calculated by:

$$\Delta m_i^{(W)} = \rho_i^{(W)} \ \Delta V_{f,i} \tag{7.36}$$

The heat transfer coefficient for water was computed similarly as for the gas in the real

Die approbierte gedruckte Originalversion dieser Diplomarbeit ist an der TU Wien Bibliothek verfügbar
The approved original version of this thesis is available in print at TU Wien Bibliothek.

gas model and was approximated by 1000 $\frac{\mathrm{W}}{\mathrm{m^2K}}$, which is again an approximation value based on the range of values given in [14], for the other two models. The heat flow into the water can be calculated with

$$\delta Q_i^{(W)} = \delta Q_i^{(W-w2)} - \delta Q_i^{(2_W)} \tag{7.37}$$

$$\approx \kappa_i^{(W,w2)}(T_i^{(w2)} - T_i^{(W)})\ (A_{total} - A_i^{(2)})\ \Delta t - \kappa_i^{(2,w)}(T_i^{(W)} - T_i^{(2)})\ r^2\pi\ \Delta t\ . \tag{7.38}$$

Then, with the heat exchange with ambient air calculated similarly as for the first vessel wall, the change of the water vessel wall temperature will be given by

$$T_{i+1}^{(w2)} = T_i^{(w2)} + \frac{(\delta Q_i^{(w2)} - \delta Q_i^{(2-w2)} - \delta Q_i^{(W-w2)})}{c_p\ m^{(w2)}}\ , \tag{7.39}$$

and, thus, the new inner energy will read

$$U_{i+1}^{(W)} = U_i^{(W)} + \delta Q_i^{(W)} + p_i^{(W)}\ \Delta V_i^c - \Delta m_i^{(W)}\ u_i^{(W)}\ . \tag{7.40}$$

For the real gas model, the pressure and inner energy can be used to calculate the new temperature and density of the water using the Helmholtz energy equation of state presented in [30] as implemented in CoolProp. For the other two models, the water was assumed to be incompressible and the temperature was calculated using

$$T_{i+1}^{(W)} = T_i^{(W)} + \frac{\delta Q_i^{(W)}}{c_W\ m_i^{(W)}}\ . \tag{7.41}$$

7.5 Algorithm

The pseudo-code in the Algorithm-1 shows a comprehensive overview of how a time step was performed in the ideal gas and van der Waals gas models, assuming all necessary information from the prior time step is given.

Die approbierte gedruckte Originalversion dieser Diplomarbeit ist an der TU Wien Bibliothek verfügbar
The approved original version of this thesis is available in print at TU Wien Bibliothek.
TU Bibliothek Your knowledge hub WIEN

Algorithm 1 Ideal gas and van der Waals gas model time step

$\gamma = \frac{5}{3}$

if $\frac{p_i^{(1)}}{p_i^{(2)}} \geq (\frac{\gamma+1}{2})^{\frac{\gamma}{\gamma-1}}$ **then**

$\psi = 1$

else

$\psi = \sqrt{\frac{2}{\gamma-1}(\frac{\gamma+1}{2})^{\frac{\gamma+1}{\gamma-1}}(\frac{p_i^{(2)}}{p_i^{(1)}})^{\frac{2}{\gamma}}(1-(\frac{p_i^{(2)}}{p_i^{(1)}})^{\frac{\gamma-1}{\gamma}})}$

end if

$\dot{m}_i = C_d\ A\ \psi\ \sqrt{\rho_i^{(1)}\ p_i^{(1)}\ \gamma(\frac{2}{\gamma+1})^{\frac{\gamma+1}{\gamma-1}}}$

if Water has not reached nozzle head **then**

$\Delta V_i^f = k_1\ \sqrt{p_i^{(2)} - p^{\text{amb}}}\ \Delta t$

else

$\Delta V_i^f = k_2\ \sqrt{p_i^{(n)} - p^{\text{amb}}}\ \Delta t$

end if

$V_{i+1}^{(2)} = V_i^{(2)} + \Delta V_i^f$

$m_{i+1}^{(1)} = m_i^{(1)} - \dot{m}_i\ \Delta t$

$m_{i+1}^{(2)} = m_i^{(2)} + \dot{m}_i\ \Delta t$

$m_{i+1}^{(W)} = m_i^{(W)} - \Delta V_i^f\ \rho^{(W)}$

$\rho_{i+1}^{(1)} = \frac{m_{i+1}^{(1)}}{V^{(1)}}$

$\rho_{i+1}^{(2)} = \frac{m_{i+1}^{(2)}}{V_{i+1}^{(2)}}$

$\Delta Q_i^{(1)} = 100\ A^{(1)}(T_i^{(w1)} - T_i^{(1)})\Delta t$

$\Delta Q_i^{(2)} = 100\ A_i^{(2)}(T_i^{(w2)} - T_i^{(2)})\Delta t + 100\ r^2\pi\ (T_i^{(W)} - T_i^{(2)})\ \Delta t$

$\Delta Q_i^{(W)} = 1000\ (A^{tot} - A_i^{(w2)})(T_i^{(\text{amb})} - T_i^{(w1)})\Delta t - 100\ r^2\pi\ (T_i^{(W)} - T_i^{(2)})\ \Delta t$

$\Delta Q_i^{(w1)} = 11\ A^{(w1)}(T_i^{(\text{amb})} - T_i^{(w1)})\Delta t - 100\ A^{(1)}(T_i^{(w1)} - T_i^{(1)})\Delta t$

$\Delta Q_i^{(w2)} = 11\ A^{(w2)}(T_i^{(\text{amb})} - T_i^{(w2)})\Delta t - 100\ A_i^{(2)}(T_i^{(w2)} - T_i^{(2)})\Delta t - 1000\ (A^{tot} - A_i^{(w2)})(T_i^{(\text{amb})} - T_i^{(w1)})\Delta t$

Die approbierte gedruckte Originalversion dieser Diplomarbeit ist an der TU Wien Bibliothek verfügbar
The approved original version of this thesis is available in print at TU Wien Bibliothek.
TU Bibliothek Your knowledge hub WIEN

$$U_{i+1}^{(1)} = U_i^{(1)} + \Delta Q_i^{(1)} - \dot{m}_i \; h_i^{(1)}$$
$$U_{i+1}^{(2)} = U_i^{(2)} + \Delta Q_i^{(2)} + \dot{m}_i \; h_i^{(1)} - p_i^{(2)} \; \Delta V_i^f$$
$$T_{i+1}^{(w1)} = T_i^{(w1)} + \frac{\Delta Q_i^{(w1)}}{c_p \; m^{(w1)}}$$
$$T_{i+1}^{(w2)} = T_i^{(w2)} + \frac{\Delta Q_i^{(w2)}}{c_p \; m^{(w2)}}$$
$$T_{i+1}^{(W)} = T_i^{(W)} + \frac{\Delta Q_i^{(W)}}{c_W \; m^{(W)}}$$

if Ideal Gas calculation **then**

$$T_{i+1}^{(1)} = \frac{2 \; U_{i+1}^{(1)} M}{3 \; k_B \; m_{i+1}^{(1)}}$$
$$T_{i+1}^{(2)} = \frac{2 \; U_{i+1}^{(2)} M}{3 \; k_B \; m_{i+1}^{(2)}}$$
$$p_{i+1}^{(1)} = \frac{\rho_{i+1}^{(1)}}{M} k_B T_{i+1}^{(1)}$$
$$p_{i+1}^{(2)} = \frac{\rho_{i+1}^{(2)}}{M} k_B T_{i+1}^{(2)}$$

else if Van der Waals calculation **then**

$$T_{i+1}^{(1)} = \frac{2 \; U_{i+1}^{(1)} \; V^{(1)} \; M^2 + a \; m_{i+1}^{2(1)}}{3 \; k_B \; m_{i+1}^{(1)} \; V^{(1)} \; M}$$
$$T_{i+1}^{(2)} = \frac{2 \; U_{i+1}^{(2)} \; V_{i+1}^{(2)} \; M^2 + a \; m_{i+1}^{2(2)}}{3 \; k_B \; m_{i+1}^{(2)} \; V_{i+1}^{(2)} \; M}$$
$$p_{i+1}^{(1)} = \frac{k_B T_{i+1}^{(1)}}{\frac{M}{\rho_{i+1}^{(1)}} - b} - \frac{a \rho_{i+1}^{2(1)}}{M^2}$$
$$p_{i+1}^{(2)} = \frac{k_B T_{i+1}^{(2)}}{\frac{M}{\rho_{i+1}^{(2)}} - b} - \frac{a \rho_{i+1}^{2(2)}}{M^2}$$

end if

if Water has reached nozzle head **then**

if $m_W > m_r$ **then**

$$p_{i+1}^{(n)} = p_{i+1}^{(2)} - \arg \min_{\Delta p \in [0, p_{i+1}^{(2)}]} f(\Delta p)$$

else

$$L_{i+1} = L_i - L \frac{\Delta V_i^f}{r_p^2 \pi L_0}$$
$$p_{i+1}^{(n)} = p_{i+1}^{(2)} - \arg \min_{\Delta p \in [0, p_{i+1}^{(2)}]} f(\Delta p)$$

end if

end if

Die approbierte gedruckte Originalversion dieser Diplomarbeit ist an der TU Wien Bibliothek verfügbar
The approved original version of this thesis is available in print at TU Wien Bibliothek.
TU Bibliothek Your knowledge hub WIEN

The pseudo-code in the Algorithm-2 shows the same for the real gas model. Note that CP stands for CoolProp, the Python package that either uses the Helmholtz equation of state or tabulated data to calculate the respective values as explained in Section 3.5. Note that an h with two superscripts is the heat transfer coefficient while an h with one superscript is the respective mass specific enthalpy.

Algorithm 2 Real gas model time step

$\gamma = CP(\rho_i^{(1)}, T_i^{(1)})$

if $\frac{p_i^{(1)}}{p_i^{(2)}} \geq (\frac{\gamma+1}{2})^{\frac{\gamma}{\gamma-1}}$ **then**

$\psi = 1$

else

$\psi = \sqrt{\frac{2}{\gamma-1}(\frac{\gamma+1}{2})^{\frac{\gamma+1}{\gamma-1}}(\frac{p_i^{(2)}}{p_i^{(1)}})^{\frac{2}{\gamma}}(1-(\frac{p_i^{(2)}}{p_i^{(1)}})^{\frac{\gamma-1}{\gamma}})}$

end if

$\dot{m}_i = C_d\ A\ \psi\ \sqrt{\rho_i^{(1)}\ p_i^{(1)}\ \gamma(\frac{2}{\gamma+1})^{\frac{\gamma+1}{\gamma-1}}}$

if Water has not reached nozzle head **then**

$\Delta V_i^f = k_1\ \sqrt{p_i^{(2)} - p^{\text{amb}}}\ \Delta t$

else

$\Delta V_i^f = k_2\ \sqrt{p_i^{(n)} - p^{\text{amb}}}\ \Delta t$

end if

$\Delta V_i^c = m_i^{(W)} \frac{\rho_i^{(W)} - \rho_{i-1}^{(W)}}{\rho_i^{(W)}\ \rho_{i-1}^{(W)}}$

$V_{i+1}^{(2)} = V_i^{(2)} + \Delta V_i^f + \Delta V_i^c$

$m_{i+1}^{(1)} = m_i^{(1)} - \dot{m}_i\ \Delta t$

$m_{i+1}^{(2)} = m_i^{(2)} + \dot{m}_i\ \Delta t$

$m_{i+1}^{(W)} = m_i^{(W)} - \Delta V_i^f\ \rho^{(W)}$

$\rho_{i+1}^{(1)} = \frac{m_{i+1}^{(1)}}{V^{(1)}}$

$\rho_{i+1}^{(2)} = \frac{m_{i+1}^{(2)}}{V_{i+1}^{(2)}}$

Die approbierte gedruckte Originalversion dieser Diplomarbeit ist an der TU Wien Bibliothek verfügbar
The approved original version of this thesis is available in print at TU Wien Bibliothek.
TU Bibliothek Your knowledge hub WIEN

for (j, k) in [(1, w1), (2, w2), (2, W), (W, w2)] **do**

$k^{(j)}, \eta^{(j)}, c_P^{(j)}, \beta^{(j)} \leftarrow CP(\rho_i^{(j)}, \frac{T_i^{(j)}+T_i^{(k)}}{2})$

$\mathrm{Pr} = \frac{c_p^{(j)}\ \eta^{(j)}}{k^{(j)}}$

$\mathrm{Gr} = \frac{9.81\ \beta^{(j)}\ \rho_i^{2(j)}\ |T_i^{(k)} - T_i^{(j)}|\ l_i^{3(j)}}{\eta^{2(j)}}$

$\mathrm{Ra} = \mathrm{Gr} \cdot \mathrm{Pr}$

if $\mathrm{Ra} \geq 10^9$ **then**

$\mathrm{Nu} = 0.13\ \mathrm{Ra}^{\frac{1}{3}}$

else if $10^4 < \mathrm{Ra} < 10^9$ **then**

$\mathrm{Nu} = 0.59\ \mathrm{Ra}^{\frac{1}{4}}$

else

$\mathrm{Nu} = 1.36\ \mathrm{Ra}^{\frac{1}{5}}$

end if

$\kappa^{(j,k)} = \frac{\mathrm{Nu}\ k^{(j)}}{l^{(j)}}$

end for

$\Delta Q_i^{(1)} = \kappa^{(1,w1)}\ A^{(1)}(T_i^{(w1)} - T_i^{(1)})\Delta t$

$\Delta Q_i^{(2)} = \kappa^{(2,w2)}\ A_i^{(2)}(T_i^{(w2)} - T_i^{(2)})\Delta t + \kappa^{(2,W)}\ r^2\pi\ (T_i^{(W)} - T_i^{(2)})\ \Delta t$

$\Delta Q_i^{(W)} = \kappa^{(W,w2)}\ (A^{tot} - A_i^{(w2)})(T_i^{(\mathrm{amb})} - T_i^{(w1)})\Delta t - \kappa^{(2,W)}\ r^2\pi\ (T_i^{(W)} - T_i^{(2)})\ \Delta t$

$\Delta Q_i^{(w1)} = 11\ A^{(w1)}(T_i^{(\mathrm{amb})} - T_i^{(w1)})\Delta t - \kappa^{(1,w1)}\ A^{(1)}(T_i^{(w1)} - T_i^{(1)})\Delta t$

$\Delta Q_i^{(w2)} = 11\ A^{(w2)}(T_i^{(\mathrm{amb})} - T_i^{(w2)})\Delta t - \kappa^{(2,w2)}\ A_i^{(2)}(T_i^{(w2)} - T_i^{(2)})\Delta t - \kappa^{(W,w12)}\ (A^{tot} - A_i^{(w2)})(T_i^{(\mathrm{amb})}$

$U_{i+1}^{(1)} = U_i^{(1)} + \Delta Q_i^{(1)} - \dot{m}_i\ h_i^{(1)}$

$U_{i+1}^{(2)} = U_i^{(2)} + \Delta Q_i^{(2)} + \dot{m}_i\ h_i^{(1)} - p_i^{(2)}\ (\Delta V_i^f\ + \Delta V_i^c)$

$U_{i+1}^{(W)} = U_i^{(W)} + \Delta Q_i^{(W)} + p_i^{(2)}\ \Delta V_i^c\ - u_i^{(W)}\ \Delta V_i^f$

$p_{i+1}^{(1)},\ T_{i+1}^{(1)} \leftarrow CP(\rho_{i+1}^{(1)}, u_{i+1}^{(1)})$

$p_{i+1}^{(2)},\ T_{i+1}^{(2)} \leftarrow CP(\rho_{i+1}^{(2)}, u_{i+1}^{(2)})$

$T_{i+1}^{(W)} \leftarrow CP(p_{i+1}^{(2)}, u_{i+1}^{(W)})$

$T_{i+1}^{(w1)} = T_i^{(w1)} + \frac{\Delta Q_i^{(w1)}}{c_p\ m^{(w1)}}$

$T_{i+1}^{(w2)} = T_i^{(w2)} + \frac{\Delta Q_i^{(w2)}}{c_p\ m^{(w2)}}\ - T_i^{(w1)})\Delta t$

Die approbierte gedruckte Originalversion dieser Diplomarbeit ist an der TU Wien Bibliothek verfügbar
The approved original version of this thesis is available in print at TU Wien Bibliothek.
TU Bibliothek Your knowledge hub WIEN

if Water has reached nozzle head **then**

if $m_W > m_r$ **then**

$$p_{i+1}^{(n)} = p_{i+1}^{(2)} - \arg \min_{\Delta p \in [0, p_{i+1}^{(2)}]} f(\Delta p)$$

else

$$L_{i+1} = L_i - L \frac{\Delta V_i^f}{r_p^2 \pi L_0}$$

$$p_{i+1}^{(n)} = p_{i+1}^{(2)} - \arg \min_{\Delta p \in [0, p_{i+1}^{(2)}]} f(\Delta p)$$

end if

end if

Die approbierte gedruckte Originalversion dieser Diplomarbeit ist an der TU Wien Bibliothek verfügbar
The approved original version of this thesis is available in print at TU Wien Bibliothek.

8 Results

In this chapter the simulation results for all three models are presented, in order of increasing complexity of the theoretical treatment, and compared with the measurement results from Chapter 5. The results of the ideal gas model are displayed in Section 8.1, the van der Waals gas model in Section 8.2 and the real gas model in Section 8.3. For each model, the data for two simulations corresponding to the two different experimental pressures of 152 and 202 bar are shown. For each experiment, the computed pressure at the different measurement points is shown in comparison to the measurement results for the whole spraying time. Due to the high gradients in the initial expansion, an additional graph shows the pressure data of the first 30 seconds of the spraying process for better visualization. Finally, the simulated gas and vessel wall temperature are displayed and compared to the measured vessel wall temperature.

8.1 Ideal Gas

Figure 8.1 shows the results of the simulation using the ideal gas model and a starting pressure of 152 bar. The actual experimental results are also plotted with dashed lines for comparison. One can see that while the temporal development of the simulation is of similar form as the experimental results, the simulated pressure from the measured pressure especially in the beginning.

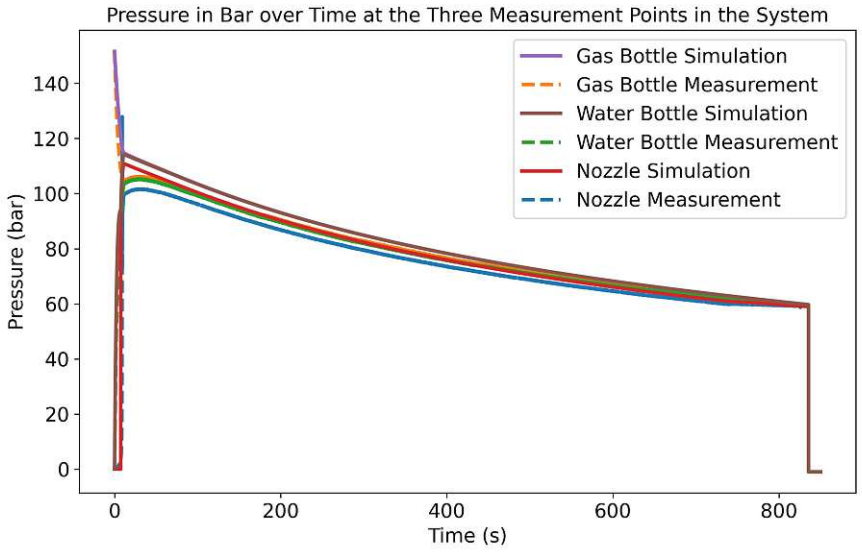

Figure 8.1: Comparison of ideal gas simulation pressure results with experiment for the 152 bar experiment.

Die approbierte gedruckte Originalversion dieser Diplomarbeit ist an der TU Wien Bibliothek verfügbar
The approved original version of this thesis is available in print at TU Wien Bibliothek.
TU Bibliothek Your knowledge hub WIEN

Because the largest deviations appear at the beginning of the process considered, Figure 8.2 shows a zoom over the first 30 seconds of simulation and experiment. The simulated gas can be seen to experience a smaller pressure drop. In addition, the calculated spraying process started about two seconds earlier than in the experiment. This is probably caused by an overestimation of the pressure in the water vessel at the beginning and the approximation of p_2 by the ambient air pressure of 1 bar in Equation (7.23). In reality, the air in the piping system is compressed, which already leads to an increase in the nozzle head pressure before the start time of the spraying process. This increase of the back pressure p_2 leads to a lower volume flow. Because of this reduced volume flow the water reaches the nozzle head later in reality. However, a higher pressure at the nozzle head leads to a higher amount of water sprayed per time interval. Thus, according to the calculations, the gas would expand and loose pressure faster than in the measurements. However, the simulation results tend to the experimental values at a later time stage with respect to the one shown in Figure 8.2.

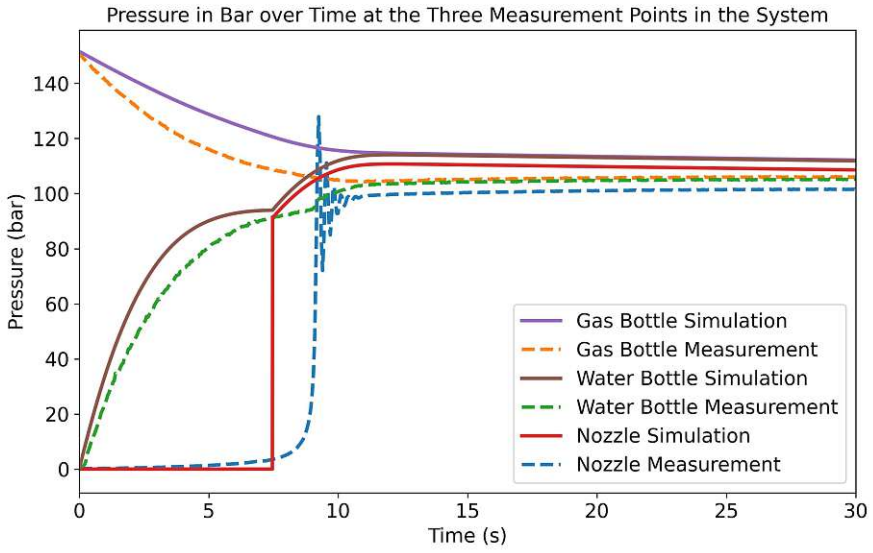

Figure 8.2: Comparison of ideal gas simulation pressure results with experiment for the first 30 seconds for the 152 bar experiment.

Figure 8.3 shows the simulated gas and gas vessel wall temperatures compared to the measured gas vessel wall temperature. Although, again, the curves appear to have overall a similar form, the experimental temperature decreases more rapidly than the simulated one. The gas temperature itself could not be measured. However, the discrepancy between the measured and simulated wall temperatures indicates that the simulated gas

Die approbierte gedruckte Originalversion dieser Diplomarbeit ist an der TU Wien Bibliothek verfügbar
The approved original version of this thesis is available in print at TU Wien Bibliothek.
TU Bibliothek Your knowledge hub WIEN

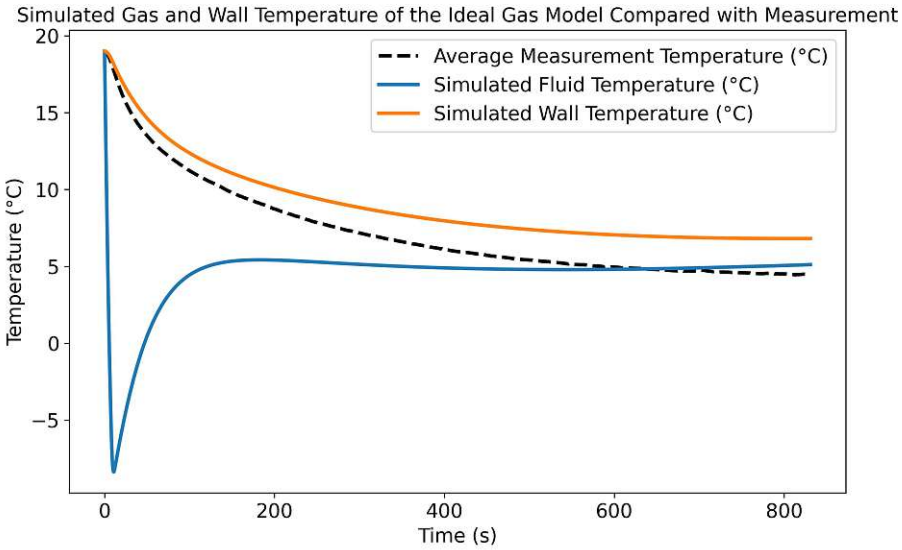

Figure 8.3: Comparison of ideal gas simulation temperature results with experiment for the 152 bar experiment.

temperature may also be correspondingly off. Figure 8.4 show the comparison of the results of the ideal gas simulation to the measurement with a starting pressure of 202 bar. While, also in this case, all the curves seem to converge as the spraying process goes on, there is a significant pressure difference at the beginning, larger than for the 152 bar experiment. Similarly as before, to better visualize this difference, Figure 8.5 shows the first 30 seconds of Figure 8.4. The simulated pressure after 10 seconds is about 20 bar too high. The reason for this behavior will be discussed in Chapter 9. However, we note that already within the first 30 seconds this difference reduces significantly. Figure 8.6 shows the comparison of the simulated gas and gas vessel wall pressure temperatures with the experimental value. Here, too, the deviations are larger than for the 152 bar starting pressure. In particular we notice that, while the actual vessel wall temperature is below zero, the simulated one is about 7 degrees Celsius higher.

Die approbierte gedruckte Originalversion dieser Diplomarbeit ist an der TU Wien Bibliothek verfügbar
The approved original version of this thesis is available in print at TU Wien Bibliothek.

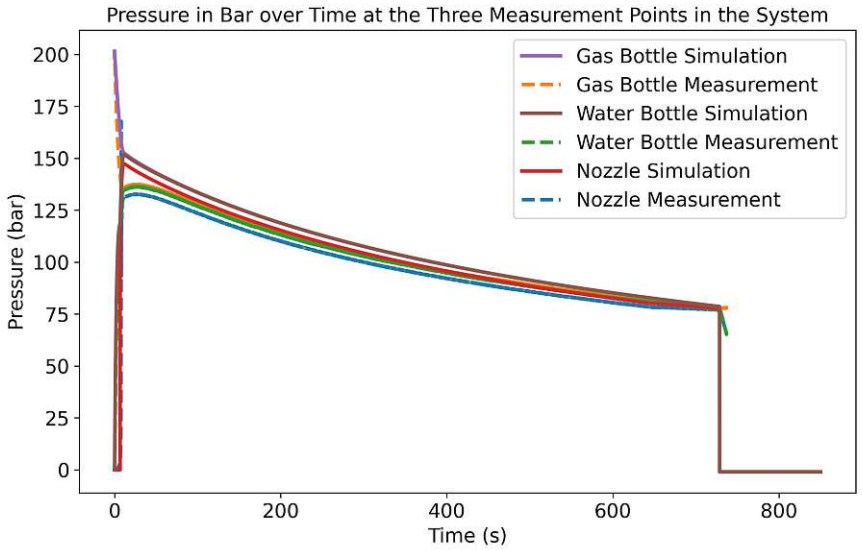

Figure 8.4: Comparison of ideal gas simulation pressure results with experiment for the 202 bar experiment.

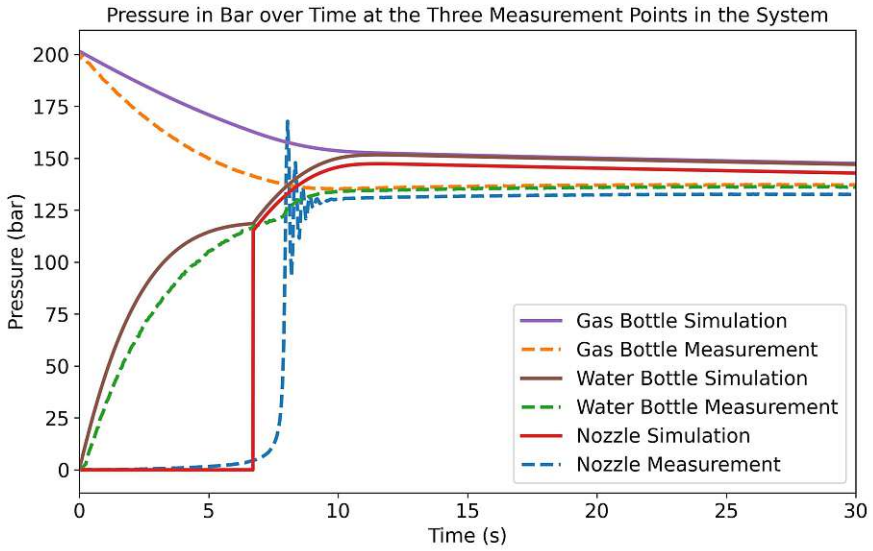

Figure 8.5: Comparison of ideal gas simulation pressure results with experiment for the first 30 seconds fo the 202 bar experiment.

Die approbierte gedruckte Originalversion dieser Diplomarbeit ist an der TU Wien Bibliothek verfügbar
The approved original version of this thesis is available in print at TU Wien Bibliothek.
TU Bibliothek Your knowledge hub WIEN

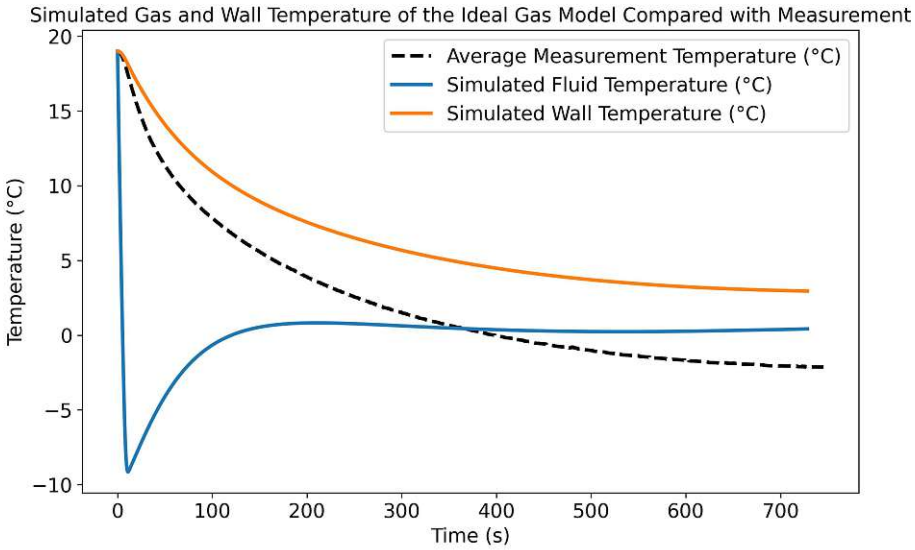

Figure 8.6: Comparison of ideal gas simulation temperature results with experiment for the 202 bar experiment.

8.2 Van der Waals Gas

Figure 8.7 shows the results of the simulation using the van der Waals gas model and a starting pressure of 152 bar. Again, the actual experimental results are plotted with dashed lines for comparison. One can see that, in this case, not only the temporal development of the simulation displays a similar form as the experimental results, but also the pressure in the beginning is much closer to the experimental values. This improvement is better visible in Figure 8.8, which shows the first 30 seconds of the simulation and experiment. Although the simulated gas still experiences a smaller pressure drop, the difference is not as large as in the ideal gas model. The improvement compared to the ideal gas model is also visible in Figure 8.9. The simulated wall temperature is much closer to the measured temperature than in the ideal gas simulation, suggesting that the simulated gas temperature might also be closer to the actual gas temperature. For a discussion of the underlying reasons, we refer the readers to Chapter 9. The improvement is also visible in the case with the starting pressure of 202 bar. Figure 8.10 shows that in this case, too, the simulated pressure gets significantly closer to the measurement. This improvement is also seen in the first 30 seconds in Figure 8.11. However, we note that with a higher starting pressure, the van der Waals gas model failed to describe the temperature as accurately as in the case with the lower starting pressure.

Die approbierte gedruckte Originalversion dieser Diplomarbeit ist an der TU Wien Bibliothek verfügbar
The approved original version of this thesis is available in print at TU Wien Bibliothek.

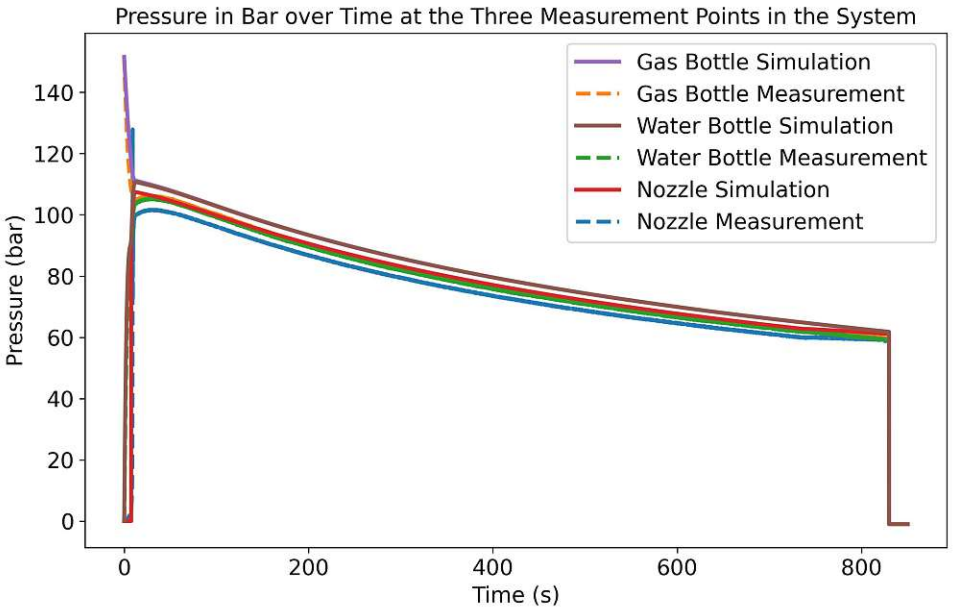

Figure 8.7: Comparison of van der Waals gas simulation pressure results with experiment for the 152 bar experiment.

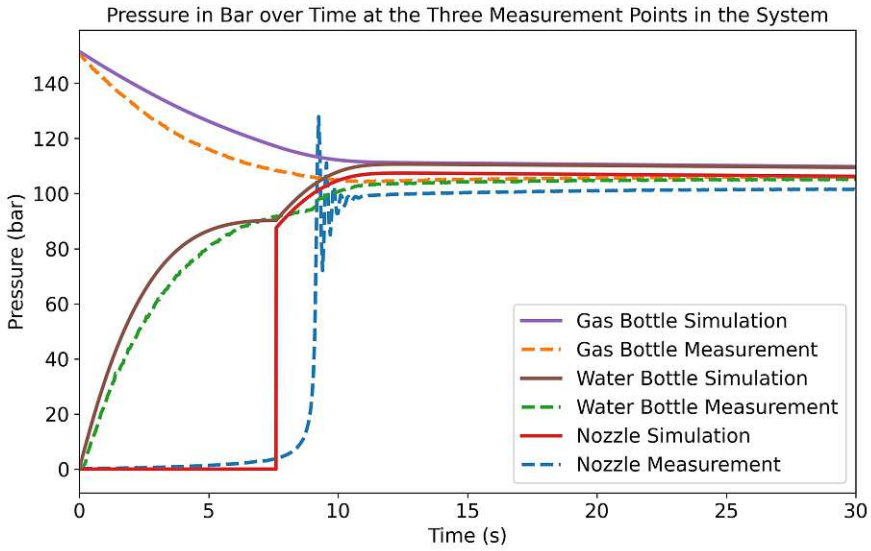

Figure 8.8: Comparison of van der Waals gas simulation pressure results with experiment for the first 30 seconds fo the 152 bar experiment.

Die approbierte gedruckte Originalversion dieser Diplomarbeit ist an der TU Wien Bibliothek verfügbar
The approved original version of this thesis is available in print at TU Wien Bibliothek.
TU Bibliothek Your knowledge hub WIEN

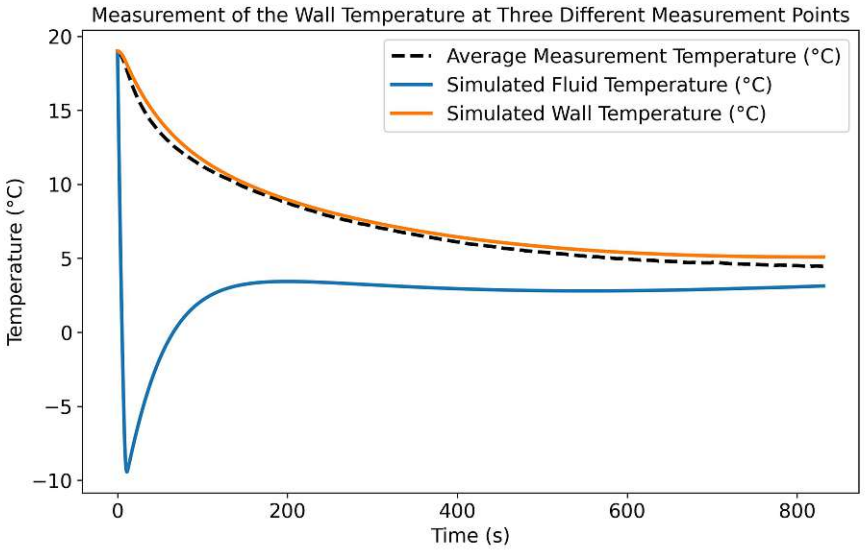

Figure 8.9: Comparison of van der Waals gas simulation temperature results with experiment for the 152 bar experiment.

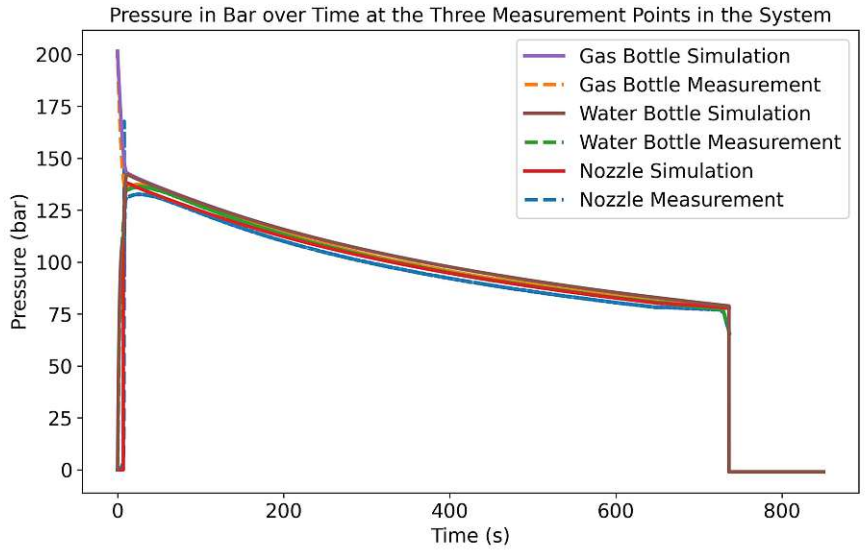

Figure 8.10: Comparison of van der Waals gas simulation pressure results with experiment for the 202 bar experiment.

Die approbierte gedruckte Originalversion dieser Diplomarbeit ist an der TU Wien Bibliothek verfügbar
The approved original version of this thesis is available in print at TU Wien Bibliothek.

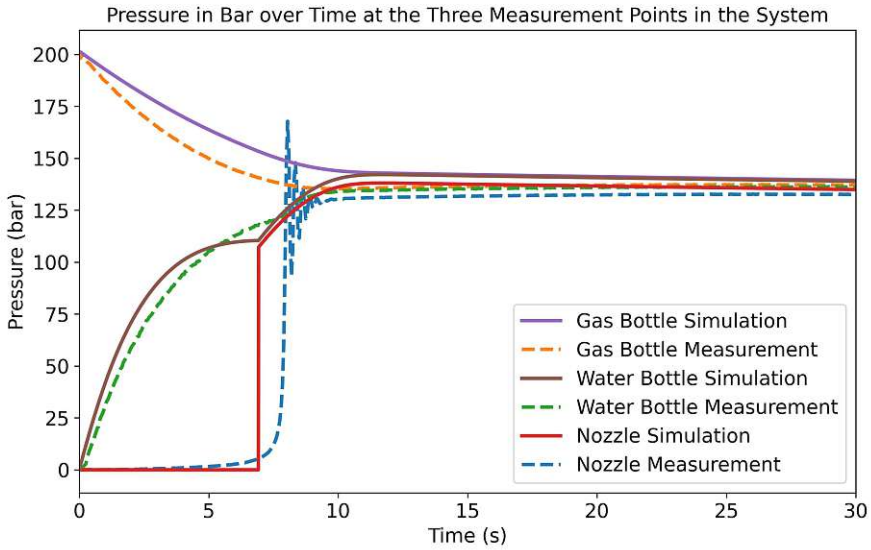

Figure 8.11: Comparison of van der Waals gas simulation pressure results with experiment for the first 30 seconds fo the 202 bar experiment.

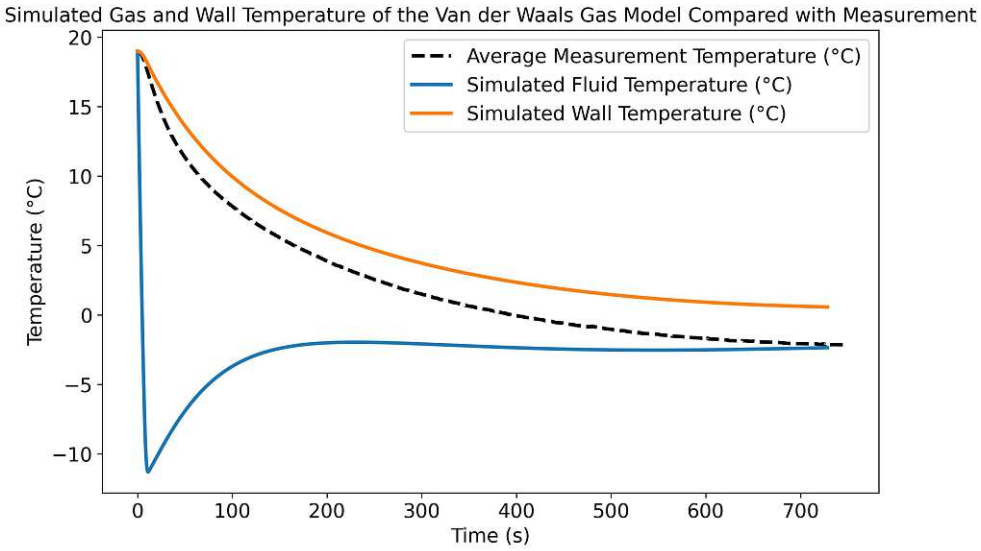

Figure 8.12: Comparison of van der Waals gas simulation temperature results with experiment for the 202 bar experiment.

Die approbierte gedruckte Originalversion dieser Diplomarbeit ist an der TU Wien Bibliothek verfügbar
The approved original version of this thesis is available in print at TU Wien Bibliothek.

8.3 Real Gas

Figure 8.13 shows, eventually, the results of the simulation performed using the real gas model and the starting pressure of 152 bar. Again, the actual experimental results are plotted with dashed lines for comparison. As expected, this model yields, overall, the best results compared to the experimental data. Such a quantitative improvement is clearly visible in Figure 8.14, which shows the first 30 seconds of the simulation and experiment, and in Figure 8.15 that shows the simulated and measured temperatures. Also in the case with a starting pressure of 202 bar, the real gas model yields the most precise performance with results very close to the actual experimental values, as it can be seen in Figure 8.16 and in Figure 8.17. Notably, with the real gas model, also in the case of a higher starting pressure, the simulation yields quite accurate results for the vessel wall temperature, which indicates a correspondingly better accuracy of the simulation of the gas temperature.

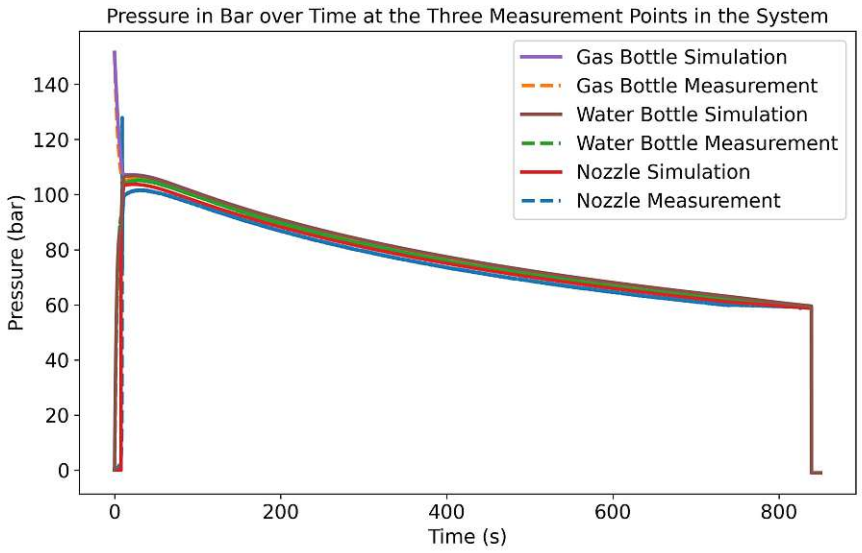

Figure 8.13: Comparison of real gas simulation pressure results with experiment for the 152 bar experiment.

Die approbierte gedruckte Originalversion dieser Diplomarbeit ist an der TU Wien Bibliothek verfügbar
The approved original version of this thesis is available in print at TU Wien Bibliothek.

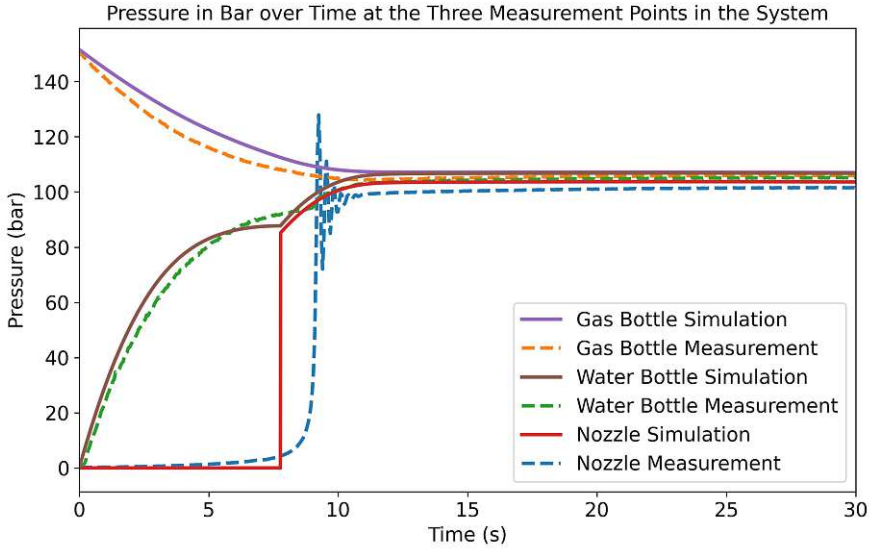

Figure 8.14: Comparison of real gas simulation pressure results with experiment for the first 30 seconds fo the 152 bar experiment.

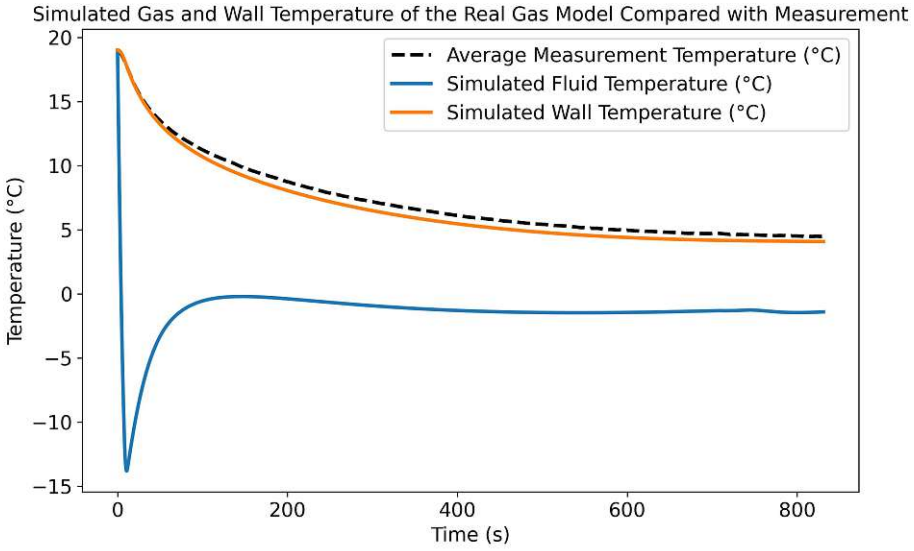

Figure 8.15: Comparison of real gas simulation temperature results with experiment for the 152 bar experiment.

Die approbierte gedruckte Originalversion dieser Diplomarbeit ist an der TU Wien Bibliothek verfügbar
The approved original version of this thesis is available in print at TU Wien Bibliothek.

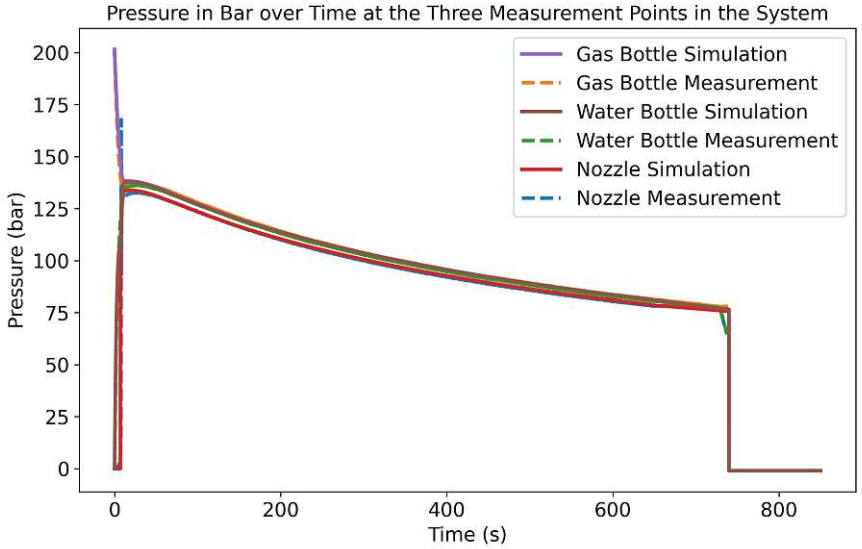

Figure 8.16: Comparison of real gas simulation pressure results with experiment for the 202 bar experiment.

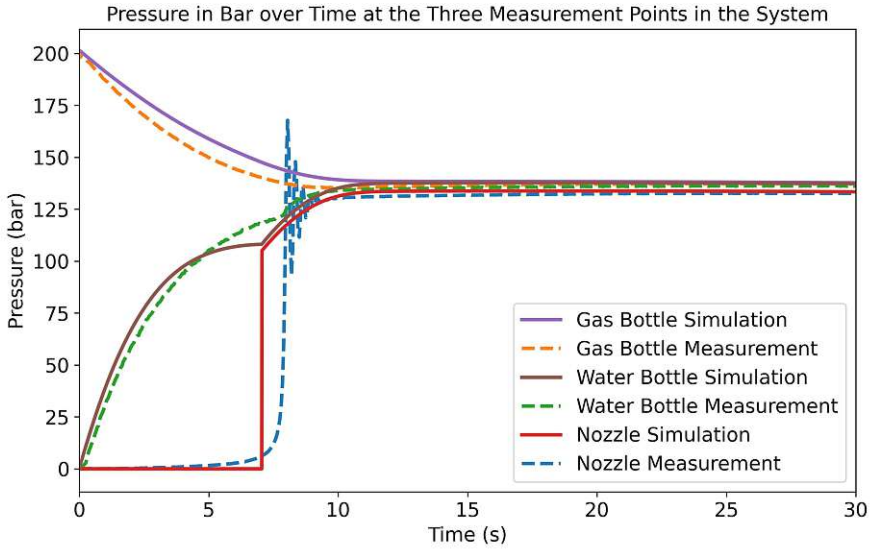

Figure 8.17: Comparison of real gas simulation pressure results with experiment for the first 30 seconds fo the 202 bar experiment.

Die approbierte gedruckte Originalversion dieser Diplomarbeit ist an der TU Wien Bibliothek verfügbar
The approved original version of this thesis is available in print at TU Wien Bibliothek.

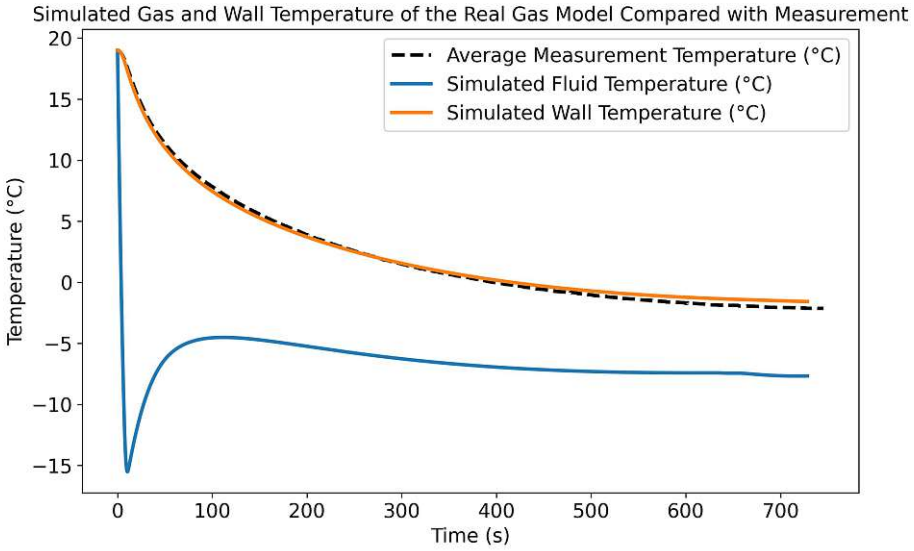

Figure 8.18: Comparison of real gas simulation temperature results with experiment for the 202 bar experiment.

Die approbierte gedruckte Originalversion dieser Diplomarbeit ist an der TU Wien Bibliothek verfügbar
The approved original version of this thesis is available in print at TU Wien Bibliothek.

9 Discussion

In this chapter the simulation results for all three models are compared and possible reasons for their different performance are considered. First, the pressure data of all three models is compared. Then, the temporal development of the inner molar energy and density for all three models is analyzed. Finally, a comparison between the van der Waals gas model and the real gas model through calculation of "effective" initial van der Waal gas parameters for the real gas model is given.

We begin our discussion by recalling that, as explained in Chapter 4, the C_d and k_v values were fitted to match the results of the system with a starting pressure of 152 bar. The fact that these values also yield good results for the system with starting pressure 202 bar indicates that the validity of these fitted values holds over a wide range of starting pressures. However, it would still be necessary to evaluate whether this is also the case for a range of different temperatures.

The data simulated with these fitted values and shown in Chapter 8 have clearly shown that, as one would expect, the real gas model performs best in predicting the temporal development of pressure and temperature in the system. In order to better quantify this aspet, Figure 9.1 shows the comparison of the simulated pressure of all the three models with the experiment at the three different measurement points in the system for a starting pressure of 152 bar. To a closer inspection, one notices that, while, especially in the first few seconds, the real gas model performs evidently best, all the curves tend to converge towards similar values. Hence, the other models appear able to provide for a gross prediction of the system behavior. Interestingly, the van der Waals gas model is better in predicting the initial pressure drop, but the convergence of the ideal gas model to the actual measurement is faster, and at some point the prediction of the ideal gas model gets closer to the measurement values than the van der Waals gas models Figure 9.2 again zooms in to the first 30 seconds, where the differences are better visible. It is important to note here that the real gas model also cannot (and does not) yield perfect results. There are a few reasons for this residual inaccuracy. First, as explained in Chapter 7, simplifications were made to describe the system. Second, classical thermodynamics uses the assumption of quasistatic processes in which the thermal subsystems are assumed to always be in thermal equilibrium. But, in our system, there is a rapid expansion in the first few seconds. Thus, it is plausible that dynamic processes partially alter the outcome. Finally, there will also be measurement uncertainties as well as inaccuracies in the experimental setup. For example, the volumes of the vessels are subject to an inaccuracy of around one percent.

Die approbierte gedruckte Originalversion dieser Diplomarbeit ist an der TU Wien Bibliothek verfügbar
The approved original version of this thesis is available in print at TU Wien Bibliothek.
TU Bibliothek Your knowledge hub WIEN

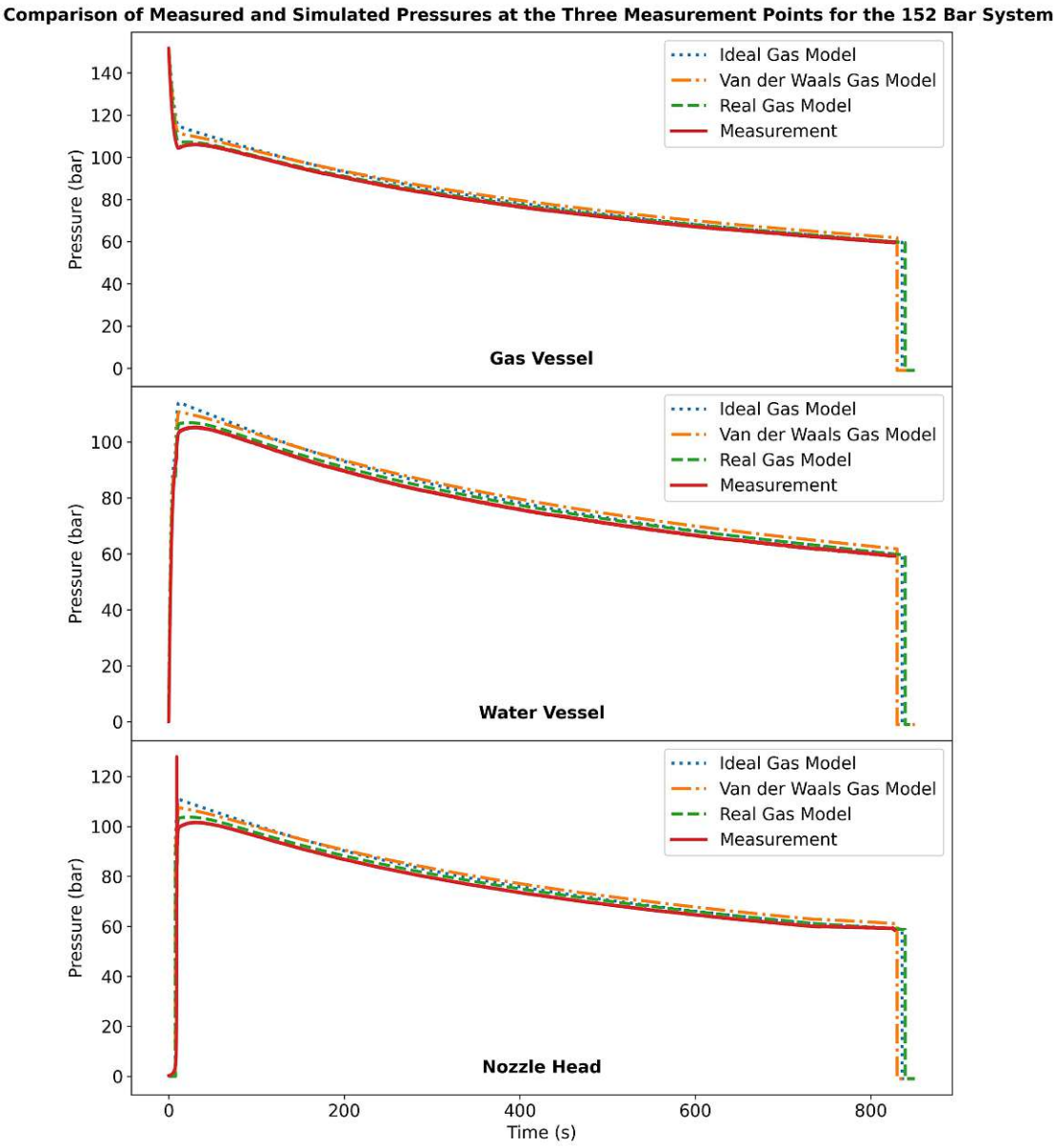

Figure 9.1: Comparison of pressures at different points in the system between measurement and the models for the 152 bar system.

Die approbierte gedruckte Originalversion dieser Diplomarbeit ist an der TU Wien Bibliothek verfügbar
The approved original version of this thesis is available in print at TU Wien Bibliothek.

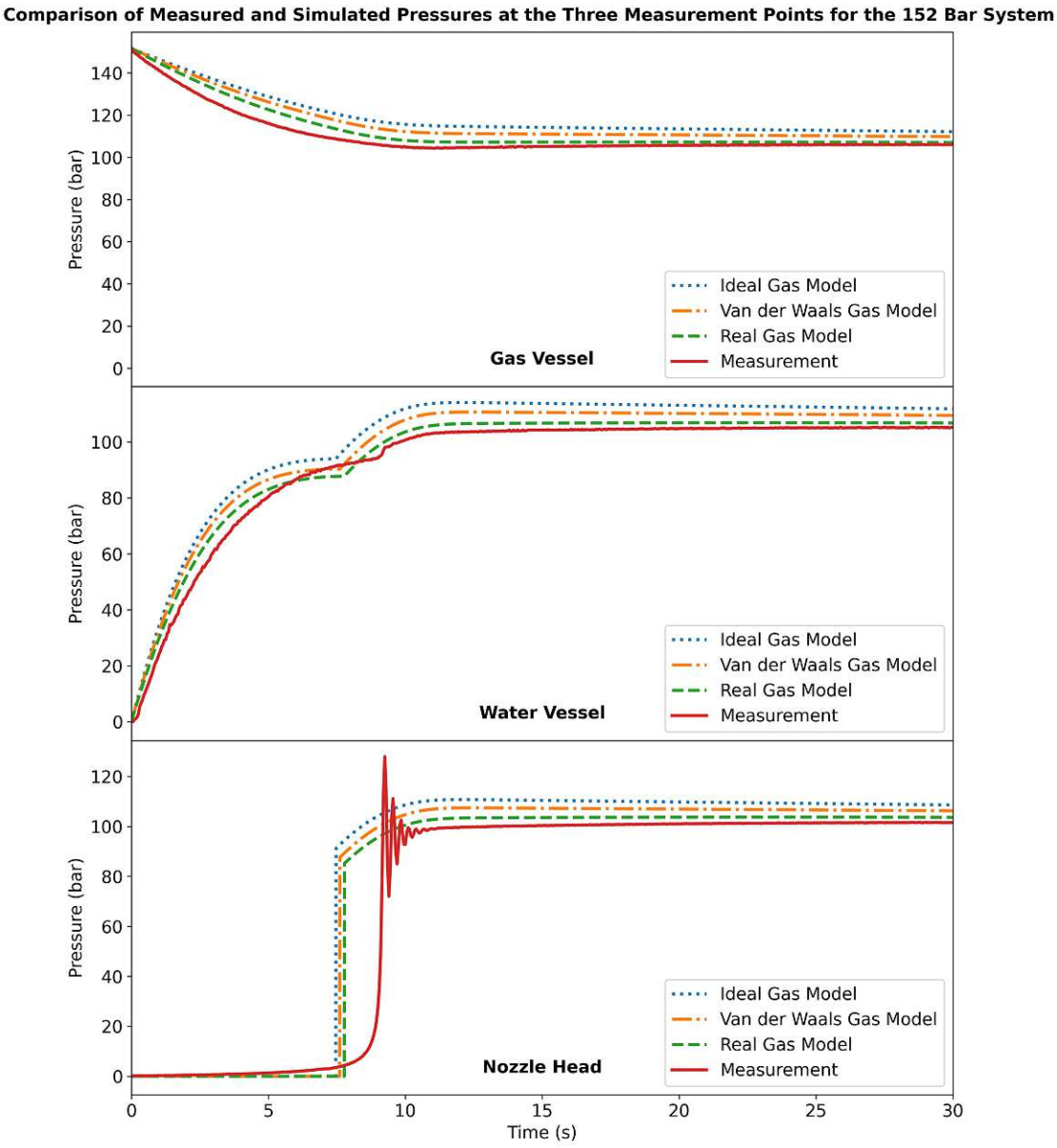

Figure 9.2: Comparison of pressures at different points in the system between measurement and the models in the first 30 seconds for the 152 bar system.

Die approbierte gedruckte Originalversion dieser Diplomarbeit ist an der TU Wien Bibliothek verfügbar
The approved original version of this thesis is available in print at TU Wien Bibliothek.

A very similar situation is visible in Figure 9.3 and Figure 9.4, which present the same data for a system with a starting pressure of 202 bar. The overall trend is similar as in the case of the lower pressure, but, in this case, the van der Waals gas model outperforms the ideal gas model throughout the whole spraying process. Due to the same reasons as for the lower pressure experiment, the real gas model again yields the best but not perfect results.

Die approbierte gedruckte Originalversion dieser Diplomarbeit ist an der TU Wien Bibliothek verfügbar
The approved original version of this thesis is available in print at TU Wien Bibliothek.

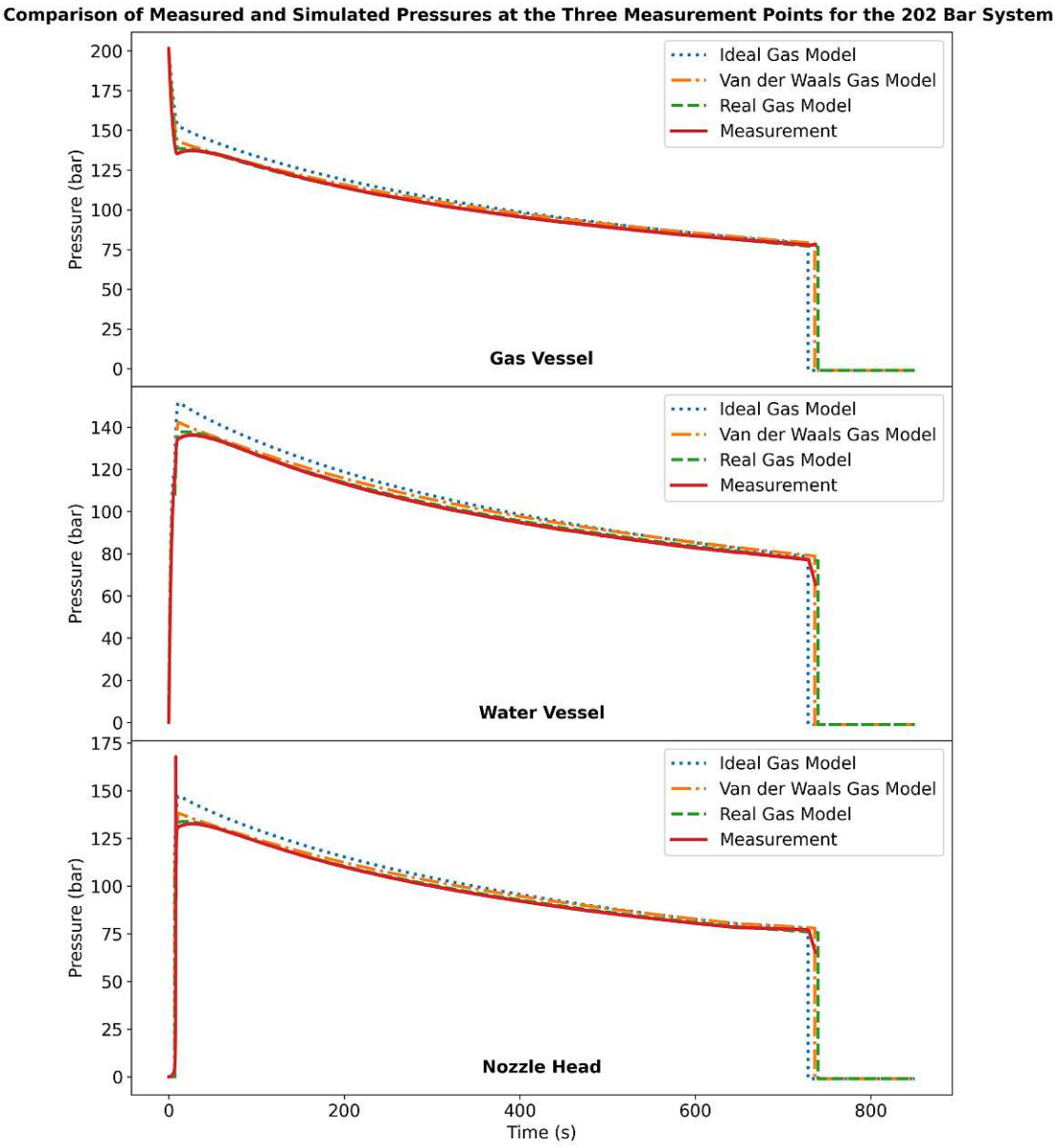

Figure 9.3: Comparison of pressures at different points in the system between measurement and the models for the 202 bar system.

Die approbierte gedruckte Originalversion dieser Diplomarbeit ist an der TU Wien Bibliothek verfügbar
The approved original version of this thesis is available in print at TU Wien Bibliothek.

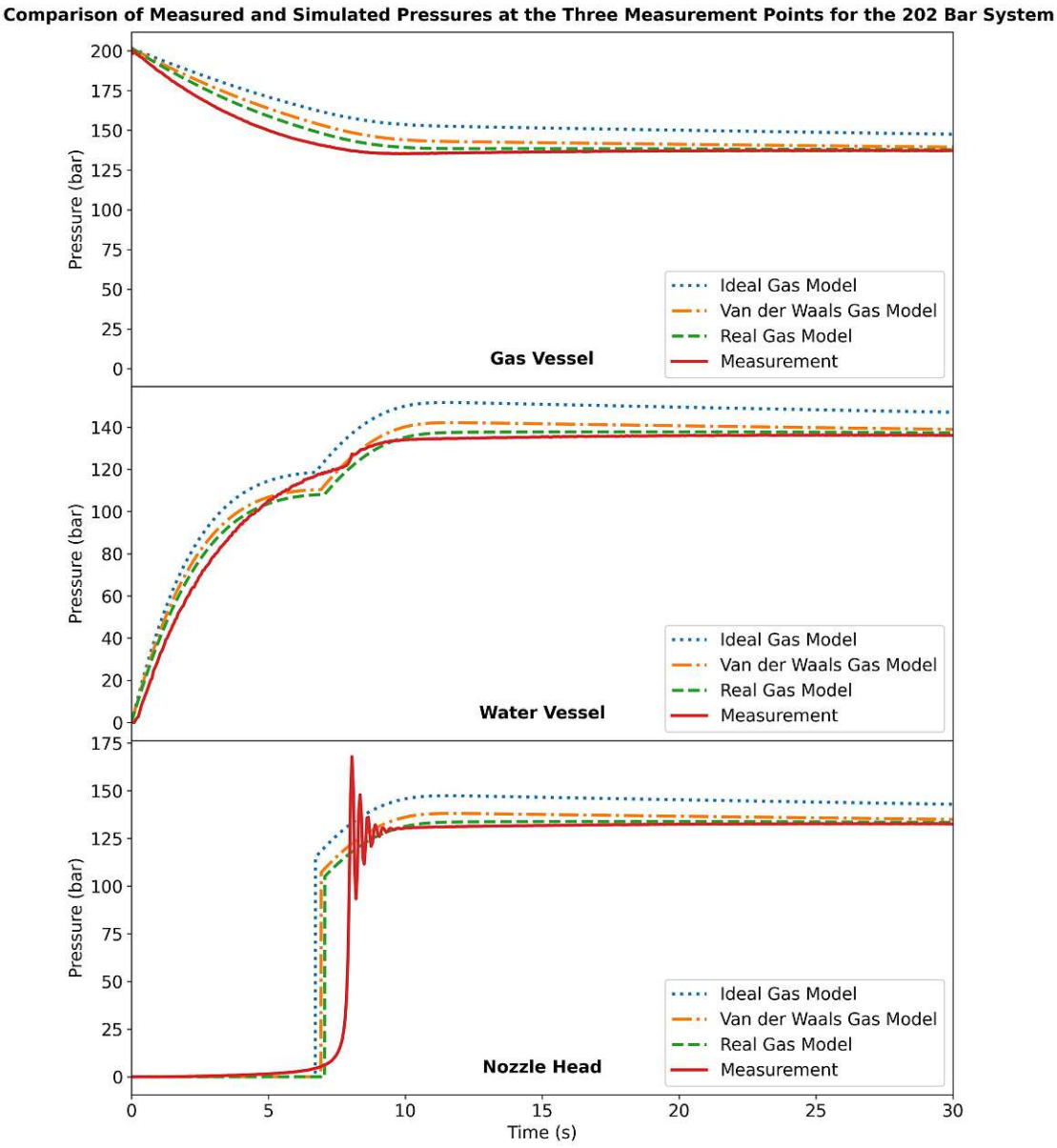

Figure 9.4: Comparison of pressures at different points in the system between measurement and the models in the first 30 seconds for the 202 bar system.

Die approbierte gedruckte Originalversion dieser Diplomarbeit ist an der TU Wien Bibliothek verfügbar
The approved original version of this thesis is available in print at TU Wien Bibliothek.

To better understand the microscopical origin of the differences between the models, the temporal development of the inner molar energy and the density have been analyzed. Figure 9.5 and Figure 9.6 show the inner molar energy over time for the three models with both starting pressures, respectively. In both cases, the ideal gas model has the highest inner molar energy followed by the van der Waals model, and the real gas model has the least inner molar energy. This reflects the behavior of the models with respect to the development of pressure over time. Because the inner molar energy for an ideal gas depends only on the temperature of the gas, the initial values of the inner molar energy for the ideal gas are identical for both starting pressures. The attractive forces between the gas atoms, instead, lead to lower inner molar energies for the higher pressure initial value in the van der Waals gas and real gas models.

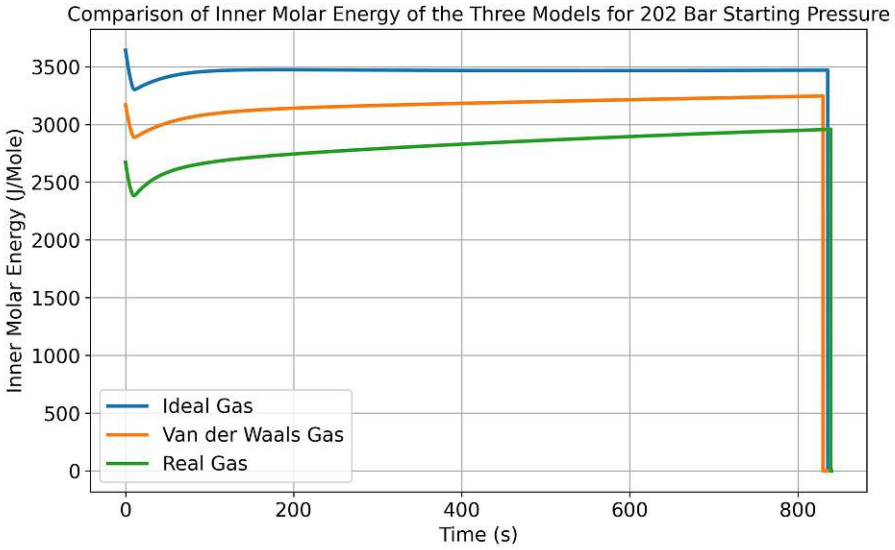

Figure 9.5: Comparison of inner molar energy of the gas between the models for the 152 bar system.

Further insight can be gained by the analysis of the temporal evolution of the gas densities in the different cases. In particular, Figure 9.7 and Figure 9.8 show the temporal development of the density for all three models over time with both starting pressures. Despite the fact that the ideal gas model has the smallest density, it yields the highest pressures in the simulation, because of the much larger inner molar energy. This nicely illustrates how the attractive interatomic forces can increase the density while simultaneously decreasing the pressure in an interacting gas.

Die approbierte gedruckte Originalversion dieser Diplomarbeit ist an der TU Wien Bibliothek verfügbar
The approved original version of this thesis is available in print at TU Wien Bibliothek.

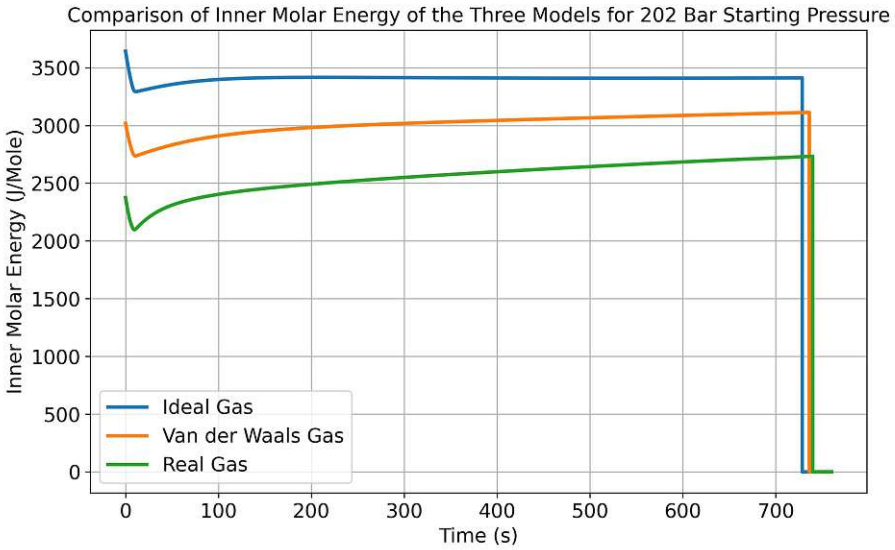

Figure 9.6: Comparison of inner molar energy of the gas between the models for the 202 bar system.

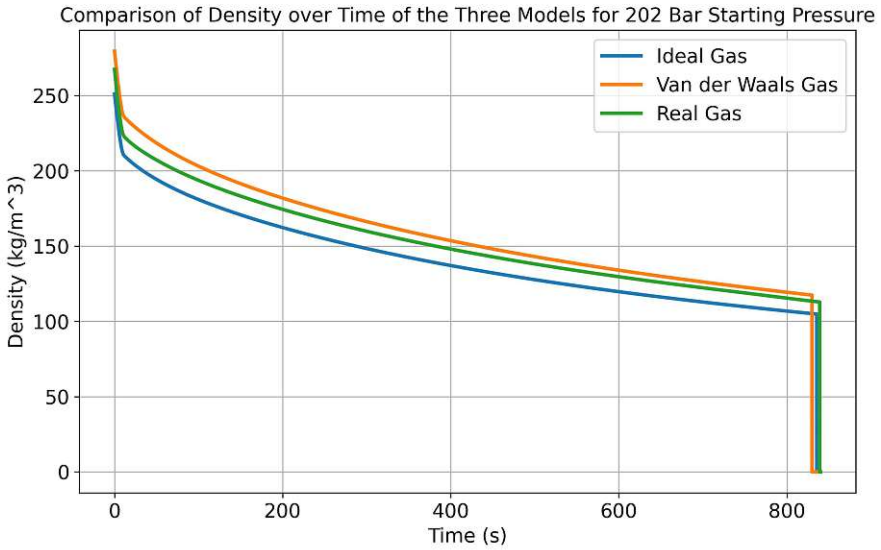

Figure 9.7: Comparison of density of the gas between the models for the 152 bar system.

Die approbierte gedruckte Originalversion dieser Diplomarbeit ist an der TU Wien Bibliothek verfügbar
The approved original version of this thesis is available in print at TU Wien Bibliothek.

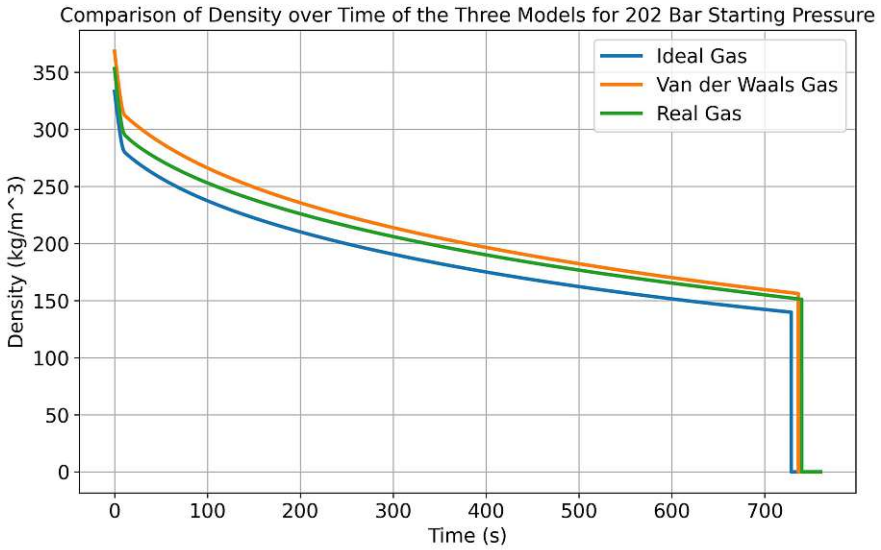

Figure 9.8: Comparison of density of the gas between the models for the 202 bar system.

In order to compare the real gas model with the van der Waals gas model in a more quantitative way, it is interesting to provide an effective estimate for the van der Waals gas parameters a and b from the real gas starting values of inner molar energy and density. In Chapter 3 it was found that for the van der Waals gas holds

$$U = U_{\text{ideal}} - \frac{a n_m^2}{V} \tag{9.1}$$

$$= \frac{3}{2} n_m RT - \frac{a n_m}{v_m} \tag{9.2}$$

$$\Rightarrow u_m = \frac{3}{2} RT - \frac{a}{v_m} \tag{9.3}$$

$$\Rightarrow a = v_m \left(\frac{3}{2} RT - u_m \right) . \tag{9.4}$$

Parameter b can be then obtained from the van der Waals equation with the calculated parameter a:

$$b = v_m - \frac{RT}{p + \frac{a}{v_m^2}} \tag{9.5}$$

Die approbierte gedruckte Originalversion dieser Diplomarbeit ist an der TU Wien Bibliothek verfügbar
The approved original version of this thesis is available in print at TU Wien Bibliothek.
TU Bibliothek Your knowledge hub WIEN

With the starting values for the system with 202 bar starting pressure, the van der Waals parameters evaluate to:

$$\tilde{a} = 0.1434 \frac{\text{Pa} \cdot \text{m}^6}{\text{mol}^2} \tag{9.6}$$

$$\tilde{b} = 3.5946 \cdot 10^{-5} \frac{\text{m}^3}{\text{mol}} \tag{9.7}$$

and for the system with starting pressure 152 bar:

$$\hat{a} = 0.1451 \frac{\text{Pa} \cdot \text{m}^6}{\text{mol}^2} \tag{9.8}$$

$$\hat{b} = 3.7826 \cdot 10^{-5} \frac{\text{m}^3}{\text{mol}} \tag{9.9}$$

On the basis of these effective estimates and their comparison with the corresponding textbook values given in Equation (3.60), we can infer some qualitative differences between the van der Waals gas and the real gas microscopic descriptions. In particular, it appears that for the initial thermodynamic state the real gas model effectively increases the attractive force represented by a and consistently lowers the inner molar energy compared to the van der Waals gas. At the same time, it also increases the "effective" value for the parameter b, which is a gross measure of the extended volume occupied by the interacting gas particles. Thus, it effectively reduces the accessible volume for the other particles, leading to a lower density of the simulated real gas compared to the van der Waals gas.

However, it is important to mention that these "effective" values for the parameters a and b are only valid for getting some theoretical insight on the comparison between the different model results at the respective pressure and temperature at which they are calculated. They should not be considered, in any aspect, an "improvement" compared to the literature values of a and b that are obtained through measurement of the critical pressure, temperature and density. In fact, any attempt to generate "effective" van der Waals gas simulation models using the "effective" values $\tilde{a}$ and $\tilde{b}$ or $\hat{a}$ and $\hat{b}$ respectively yielded far worse results than all of the three models considered prior in this thesis. This illustrates that two parameters are just too few to accurately describe real gas effects over a wide range of pressures or temperatures.

Die approbierte gedruckte Originalversion dieser Diplomarbeit ist an der TU Wien Bibliothek verfügbar
The approved original version of this thesis is available in print at TU Wien Bibliothek.
TU Bibliothek Your knowledge hub WIEN

10 Summary and Outlook

In this work three numerical models were developed to predict the pressure and temperature of a fire extinguishing system driven by a gas-powered power pack. They were based on the ideal gas law, the van der Waals gas law, and a real gas model using an experimentally fitted Helmholtz equation of state and tabulated data. For all models, the fire extinguishing system was divided into three thermodynamic subsystems. In each timestep, the mass flow and the energy flow between these systems were computed and the thermodynamic states were updated using the respective thermodynamic laws. The performance of these models was evaluated by comparing their predictions with measured data from two experiments at different starting system pressures performed in the facilities of AQUASYS TECHNIK GMBH in Linz under the supervision of the author.

All three models were able to produce reasonable predictions for the fundamental physical variable controlling the systems time evolution, namely the temporal development of the system pressure. Due to the dependence of the water outflow on the system pressure the predictions of the models and the actual measurement tend to reach their asymptotic value, controlled by the ambient air pressure, over different time scales. Consequently, the larger deviations between the model predictions and experiments are found in the initial part of the process and decline over time. As expected, by quantitatively comparing with the measured values of the pressure, the real gas model displayed the best performance followed by the van der Waals gas model with the ideal gas model yielding overall less accurate predictions. Still, because of approximations, the dynamic nature of the expansion process and possible measurement errors as well as inaccuracies in the setup of the experiments the real gas model also did not yield perfect predictions for the measured values. To account for dynamic effects, and further improving the quantitative agreement, a computational fluid dynamics simulation, which is clearly beyond the scope of this Master thesis work, would be necessary.

On a more microscopical perspective, further analysis has shown that the van der Waals gas model underestimates the attractive as well as the repulsive forces in the initial high-pressure setting of our system. This observation, while useful for the physical interpretation of the numerical results, cannot be exploited, however, for effectively improving the performance of the van der Waals model. In fact, attempts to build "effective" van der Waals gas simulation models by fitting the parameters a and b to the real gas starting densities and inner molar energies yielded bad predictions when compared to the original three models, showing that two parameters are too few to accurately describe real gas behavior over a wide range of pressures and temperatures.

Finally, it is important to recall that only the simplest form of a GPP firefighting system was simulated in this thesis work. For industrial use, it would be necessary to further

Die approbierte gedruckte Originalversion dieser Diplomarbeit ist an der TU Wien Bibliothek verfügbar
The approved original version of this thesis is available in print at TU Wien Bibliothek.
TU Bibliothek Your knowledge hub WIEN

evaluate the performance of the real gas model when extended to more complicated systems including multiple gas vessels, water vessels, or nozzle heads in serial or parallel arrangements. In this context, it may become necessary to resort to CFD simulations for these geometrically more complicated systems. Furthermore, argon, which has been used here for both experiments, is a noble gas. Thus, for other operating gases, such as nitrogen, additional, possibly stronger interaction effects might further lower the model abilities to predict the temporal development of pressure over time. To summarize, this thesis should be seen as a proof of principle and a starting point to further develop simulations for more complicated systems. Developing such a procedure has the potential to significantly reduce the trial-and-error steps in the layout of a firefighting system, making the realization of more powerful GPP systems, without pressure reducing valves, economically feasible.

Die approbierte gedruckte Originalversion dieser Diplomarbeit ist an der TU Wien Bibliothek verfügbar
The approved original version of this thesis is available in print at TU Wien Bibliothek.
TU Bibliothek Your knowledge hub WIEN

Declaration on the usage of AI in the writing process

The Writefull language model has been used to proofread this work. The use was limited to spelling and grammar checks and stylistic recommendations. No text passages were generated. Each recommendation has been carefully reviewed to ensure precision and clarity.

Die approbierte gedruckte Originalversion dieser Diplomarbeit ist an der TU Wien Bibliothek verfügbar
The approved original version of this thesis is available in print at TU Wien Bibliothek.

References

1. European Parliament, Council of the European Union. Directive (EU) 2016/797 of the European Parliament and of the Council of 11 May 2016 on the interoperability of the rail system within the European Union. Accessed: 2025-03-01. 2016. https://eur-lex.europa.eu/legal-content/EN/ALL/?uri=CELEX:32016L0797.
2. European Union Agency for Railways. Technical Specifications for Interoperability (TSIs). Accessed: 2025-03-10. https://www.era.europa.eu/domains/technical-specifications-interoperability_en.
3. ARGE. ARGE-Richtlinie - Teil 2: Brandbekämpfung in Schienenfahrzeugen. Accessed: 2025-03-13. https://www.tuvsud.com/de-de/-/media/de/rail/pdf/arge-richtlinien/arge-richtlinie---teil-2-brandbekaempfung-in-schienenfahrzeugen.pdf.
4. Demtröder, W. Experimentalphysik 1 - Mechanik und Wärme 7th edition. ISBN: 978-3-662-46414-4 (Springer-Verlag, Berlin Heidelberg, 2015).
5. Toschi, A. Statistische Physik II. Power Point slides, TU Wien. 2024.
6. Schwabl, F. Statistische Mechanik 3rd edition. ISBN: 978-3-540-31097-6 (Springer-Verlag, Berlin Heidelberg, 2006).
7. Nolting, W. Grundkurs Theoretische Physik 6 7th edition. ISBN: 978-3-642-25392-8 (Springer-Verlag, Berlin Heidelberg, 2013).
8. Van Dongen, P. Statitische Physik 1st edition. ISBN: 978-3-662-55499-9 (Springer-Verlag, Berlin Heidelberg, 2017).
9. Di Castro, C. & Raimondi, R. Statistical Mechanics and Applications in Condensed Matter 1st edition. ISBN: 9781139600286 (Cambridge University Press, Cambridge, 2015).
10. Tegeler, C., Span, R. & Wagner, W. A New Equation of State for Argon Covering the Fluid Region for Temperatures From the Melting Line to 700 K at Pressures up to 1000 MPa. *Journal of Physical and Chemical Reference Data* **28.** https://doi.org/10.1063/1.556037 (1999).
11. Andreasen, A. HydDown: A Python package for calculation of hydrogen (or other gas) pressure vessel filling and discharge. *Journal of Open Source Software* **6,** 3695. https://doi.org/10.21105/joss.03695 (2021).
12. Atkins, P. & de Paula, J. Atkins' Physical Chemistry 9th edition (Oxford University Press, Oxford, UK, 2010).

Die approbierte gedruckte Originalversion dieser Diplomarbeit ist an der TU Wien Bibliothek verfügbar
The approved original version of this thesis is available in print at TU Wien Bibliothek.
TU Bibliothek Your knowledge hub WIEN

13. Bell, I. H., Wronski, J., Quoilin, S. & Lemort, V. Pure and Pseudo-pure Fluid Thermophysical Property Evaluation and the Open-Source Thermophysical Property Library CoolProp. *Industrial & Engineering Chemistry Research* **53,** 2498–2508. eprint: http://pubs.acs.org/doi/pdf/10.1021/ie4033999. http://pubs.acs.org/doi/abs/10.1021/ie4033999 (2014).
14. VDI-Wärmeatlas 11th edition (ed VDI-Gesellschaft Verfahrenstechnik und Chemieingenieurwesen (GVC)) ISBN: 978-3-642-19980-6 (Springer-Verlag, Wiesbaden, 2013).
15. Geankoplis, C. Transport Processes and Unit Operations. ISBN: 9780205059393. https://books.google.at/books?id=p8FTAAAAMAAJ (Allyn and Bacon, 1978).
16. Lemmon, E. W., Bell, I. H., Huber, M. L. & McLinden, M. O. Thermophysical Properties of Fluid Systems in NIST Chemistry WebBook, NIST Standard Reference Database Number 69 (eds Linstrom, P. J. & Mallard, W. G.) Accessed: 2025-02-17. Gaithersburg, MD, 20899. https://doi.org/10.18434/T4D303.
17. Woodfield, P. L., Monde, M. & Mitsutake, Y. Measurement of Averaged Heat Transfer Coefficients in High-Pressure Vessel during Charging with Hydrogen, Nitrogen or Argon Gas. *Journal of Thermal Science and Technology* **2,** 180–191 (2007).
18. Methods for the Calculation of Physical Effects (Yellow Book) – CPR 14E 3rd (eds van den Bosch, C. J. H. & Weterings, R. A. P. M.) (Committee for the Prevention of Disasters, 2005).
19. Manhartsgruber, B. Pneumatik. Vorlesungsskript, Institut für Maschinenlehre und hydraulische Antriebstechnik, Johannes Kepler Universität Linz. Stand: 11.12.2008. 2008.
20. Brown, G. O. in *Environmental and Water Resources History* 34–43 (). eprint: https://ascelibrary.org/doi/pdf/10.1061/40650%282003%294. https://ascelibrary.org/doi/abs/10.1061/40650%282003%294.
21. VdS Schadenverhütung GmbH. VdS-Richtlinien für Wassernebelsysteme – VdS 3188: Wassernebel-Sprinkleranlagen und Wassernebel-Löschanlagen (Hochdruck-Systeme). Köln, 2019.
22. National Fire Protection Association. NFPA 750: Standard on Water Mist Fire Protection Systems. Quincy, MA. 2015.
23. Huber, M. L. *et al.* New International Formulation for the Viscosity of H2O. *Journal of Physical and Chemical Reference Data* **38,** 101–125. ISSN: 0047-2689. eprint: https://pubs.aip.org/aip/jpr/article-pdf/38/2/101/16735949/101_1_online.pdf. https://doi.org/10.1063/1.3088050 (2009).
24. Auer, M. Ein Beitrag zur Erhöhung der Reichweite eines batterieelektrischen Fahrzeugs durch prädiktives Thermomanagement. ISBN: 978-3-658-13208-8. https://link.springer.com/book/10.1007/978-3-658-13209-5 (Springer Vieweg, Wiesbaden, 2016).

Die approbierte gedruckte Originalversion dieser Diplomarbeit ist an der TU Wien Bibliothek verfügbar
The approved original version of this thesis is available in print at TU Wien Bibliothek.
TU Bibliothek Your knowledge hub WIEN

25. Atkinson, K. E. An Introduction to Numerical Analysis 2nd Edition. ISBN: 0471500232. http://www.worldcat.org/isbn/0471500232 (John Wiley & Sons, New York, 1989).

26. Coursey, J. S., Schwab, D. J., Tsai, J. J. & Dragoset, R. A. Atomic Weights and Isotopic Compositions (version 4.1). http://physics.nist.gov/Comp. National Institute of Standards and Technology, Accessed: 2025-05-05. Gaithersburg, MD. 2015.

27. Virtanen, P. *et al.* SciPy 1.0: Fundamental Algorithms for Scientific Computing in Python. *Nature Methods* **17,** 261–272 (2020).

28. Gao, F. & Han, L. Implementing the Nelder-Mead simplex algorithm with adaptive parameters. *Computational Optimization and Applications* **51,** 259–277. https://doi.org/10.1007/s10589-010-9329-3 (2012).

29. Sochacki, J. S. Introduction to Compressible Computational Fluid Dynamics. http://www.math.jmu.edu/~jim/compressible.html. James Madison University, Accessed: 2025-06-13.

30. Wagner, W. & Pruß, A. The IAPWS Formulation 1995 for the Thermodynamic Properties of Ordinary Water Substance for General and Scientific Use. *Journal of Physical and Chemical Reference Data* **31** (2002).

Die approbierte gedruckte Originalversion dieser Diplomarbeit ist an der TU Wien Bibliothek verfügbar
The approved original version of this thesis is available in print at TU Wien Bibliothek.
TU Bibliothek Your knowledge hub WIEN